

# Generative AI Enables Medical Image Segmentation in Ultra Low-Data Regimes

Li Zhang<sup>1</sup>, Basu Jindal<sup>1</sup>, Ahmed Alaa<sup>2,3</sup>, Robert Weinreb<sup>4</sup>, David Wilson<sup>5</sup>, Eran Segal<sup>6,7</sup>, James Zou<sup>8,9</sup>, and Pengtao Xie<sup>1,10</sup> ✉

<sup>1</sup>Department of Electrical and Computer Engineering, University of California San Diego, La Jolla, CA, USA

<sup>2</sup>Baker Computational Health Sciences Institute, University of California San Francisco, San Francisco, CA, USA

<sup>3</sup>Department of Electrical Engineering and Computer Sciences, University of California Berkeley, Berkeley, CA, USA

<sup>4</sup>Hamilton Glaucoma Center, Shiley Eye Institute, Viterbi Family Department of Ophthalmology, University of California San Diego, La Jolla, CA, USA

<sup>5</sup>Division of Pulmonary, Allergy and Critical Care Medicine, Department of Medicine, University of Pittsburgh, Pittsburgh, PA, USA

<sup>6</sup>Department of Computer Science and Applied Mathematics, Weizmann Institute of Science, Rehovot, Israel

<sup>7</sup>Department of Molecular Cell Biology, Weizmann Institute of Science, Rehovot, Israel

<sup>8</sup>Department of Biomedical Data Science, Stanford University School of Medicine, Stanford, CA, USA

<sup>9</sup>Department of Computer Science, Stanford University, Stanford, CA, USA

<sup>10</sup>Department of Medicine, University of California San Diego, La Jolla, CA, USA

Semantic segmentation of medical images is pivotal in applications like disease diagnosis and treatment planning. While deep learning has excelled in automating this task, a major hurdle is the need for numerous annotated segmentation masks, which are resource-intensive to produce due to the required expertise and time. This scenario often leads to ultra low-data regimes, where annotated images are extremely limited, posing significant challenges for the generalization of conventional deep learning methods on test images. To address this, we introduce a generative deep learning framework, which uniquely generates high-quality paired segmentation masks and medical images, serving as auxiliary data for training robust models in data-scarce environments. Unlike traditional generative models that treat data generation and segmentation model training as separate processes, our method employs multi-level optimization for end-to-end data generation. This approach allows segmentation performance to directly influence the data generation process, ensuring that the generated data is specifically tailored to enhance the performance of the segmentation model. Our method demonstrated strong generalization performance across 9 diverse medical image segmentation tasks and on 16 datasets, in ultra-low data regimes, spanning various diseases, organs, and imaging modalities. When applied to various segmentation models, it achieved performance improvements of 10-20% (absolute), in both same-domain and out-of-domain scenarios. Notably, it requires 8 to 20 times less training data than existing methods to achieve comparable results. This advancement significantly improves the feasibility and cost-effectiveness of applying deep learning in medical imaging, particularly in scenarios with limited data availability.

Medical image segmentation | Generative AI | Ultra low-data regimes | End-to-end data generation

Correspondence: [p1xie@ucsd.edu](mailto:p1xie@ucsd.edu)

## Introduction

Medical image semantic segmentation (1–3) is a pivotal process in the modern healthcare landscape, playing an indispensable role in diagnosing diseases (4), tracking disease progression (5), planning treatments (6), assisting surgeries (7), and supporting numerous other clinical activities (8, 9). This process involves classifying each pixel within a specific image, such as a skin dermoscopy image, with a corresponding semantic label, such as skin cancer or normal skin.

The advent of deep learning has revolutionized this domain, offering unparalleled precision and automation in the segmentation of medical images (1, 2, 10, 11). Despite these advancements, training accurate and robust deep learning models requires extensive, annotated medical imaging datasets, which are notoriously difficult to obtain (9, 12). Labeling semantic segmentation masks for medical images is both time-intensive and costly, as it necessitates annotating each pixel. It requires not only substantial human resources but also specialized domain expertise. This leads to what is termed as *ultra low-data regimes* – scenarios where the availability of annotated training images is remarkably scarce. This scarcity poses a substantial challenge to the existing deep learning methodologies, causing them to overfit to training data and exhibit poor generalization performance on test images.

To address the scarcity of labeled image-mask pairs in semantic segmentation, several strategies have been devised, including data augmentation and semi-supervised learning approaches. Data augmentation techniques (13–16) create synthetic pairs of images and masks, which are then utilized as supplementary training data. A significant limitation of these methods is that they treat data augmentation and segmentation model training as separate activities. Consequently, the process of data augmentation is not influenced by segmentation performance, leading to a situation where the augmented data might not contribute effectively to enhancing the model’s segmentation capabilities. Semi-supervised learning techniques (8, 17–20) exploit additional, unlabeled images to bolster segmentation accuracy. Despite their potential, these methods face limitations due to the necessity for extensive volumes of unlabeled images, a requirement often difficult to fulfill in medical settings where even unlabeled data can be challenging to obtain due to privacy issues, regulatory hurdles (e.g., IRB approvals), among others.

Recognizing these critical gaps, we introduce a new approach - GenSeg - that leverages generative deep learning (21–23) to address the challenges posed by ultra low-data regimes. Our approach is capable of generating high-fidelity paired segmentation masks and medical im-

057 ages. This auxiliary data facilitates the training of accurate  
058 segmentation models in scenarios with extremely limited  
059 real data. What sets our approach apart from existing data  
060 generation/augmentation methods (13–16) is its unique  
061 capability to facilitate end-to-end data generation through  
062 multi-level optimization (24). The data generation process  
063 is intricately guided by segmentation performance, ensuring  
064 that the generated data is not only of high quality but  
065 also specifically optimized to enhance the segmentation  
066 model’s performance. Furthermore, in contrast to semi-  
067 supervised segmentation tools (8, 17–20), our method  
068 eliminates the need for additional unlabeled images, which  
069 are often challenging to acquire. GenSeg is a versatile,  
070 model-independent framework designed to enhance the  
071 performance of a wide range of segmentation models when  
072 integrated with them.

073  
074 GenSeg was validated across 9 segmentation tasks on  
075 16 datasets, covering an extensive variety of imaging  
076 modalities, diseases, and organs. When integrated with  
077 UNet (25) and DeepLab (10) in ultra low-data regimes  
078 (for instance, with only 50 training examples), GenSeg  
079 significantly enhanced their performance, in both same-  
080 domain scenarios (where training and testing images come  
081 from the same distribution) and out-of-domain scenarios  
082 (where training and testing images originate from different  
083 distributions), achieving performance gains of 10-20%  
084 (absolute percentages) in most cases. GenSeg is highly  
085 data efficient, outperforming or matching the segmentation  
086 performance of baseline methods with 8-20 times fewer  
087 training examples.

## 088 Results

089 **GenSeg overview.** GenSeg is an end-to-end data genera-  
090 tion framework designed to generate high-quality, labeled  
091 data, to enable the training of accurate medical image  
092 segmentation models in ultra low-data regimes (Fig. 1a).  
093 Our framework integrates two components: a data genera-  
094 tion model and a semantic segmentation model. The data  
095 generation model is responsible for generating synthetic  
096 pairs of medical images and their corresponding segmen-  
097 tation masks. This generated data serves as the training  
098 material for the segmentation model. In our data generation  
099 process, we introduce a reverse generation mechanism. This  
100 mechanism initially generates segmentation masks, and  
101 subsequently, medical images, adhering to a progression  
102 from simpler to more complex tasks. Specifically, given an  
103 expert-annotated real segmentation mask, we apply basic  
104 image augmentation operations to produce an augmented  
105 mask, which is then inputted into a deep generative model  
106 to generate the corresponding medical image. A key distinc-  
107 tion of our method lies in the architecture of this generative  
108 model. Unlike traditional models (22, 23, 26, 27) that rely  
109 on manually designed architecture, our model automatically  
110 learns this architecture from data (Fig. 1b). This adaptive  
111 architecture enables more nuanced and effective generation  
112  
113

of medical images, tailored to the specific characteristics of  
the augmented segmentation masks.

GenSeg features an end-to-end data generation strat-  
egy, which ensures a synergistic relationship between the  
generation of data and the performance of the segmentation  
model. By closely aligning the data generation process with  
the needs and feedback of the segmentation model, GenSeg  
ensures the relevance and utility of the generated data for  
effective training of the segmentation model. To evaluate the  
effectiveness of the generated data, we first train a semantic  
segmentation model using this data. We then assess the  
model’s performance on a validation set consisting of real  
medical images, each accompanied by an expert-annotated  
segmentation mask. The model’s validation performance  
serves as a reflection of the quality of the generated data: if  
the data is of low quality, the segmentation model trained  
on it will show poor performance during validation. By  
concentrating on improving the model’s validation perfor-  
mance, we can, in turn, enhance the quality of the generated  
data.

Our approach utilizes a multi-level optimization (MLO) (24)  
strategy to achieve end-to-end data generation. MLO  
involves a series of nested optimization problems, where the  
optimal parameters from one level serve as inputs for the  
objective function at the next level. Conversely, parameters  
that are not yet optimized at a higher level are fed back  
as inputs to lower levels. This yields a dynamic, iterative  
process that solves optimization problems in different  
levels jointly. Our method employs a three-tiered MLO  
process, executed end-to-end. The first level focuses on  
training the weight parameters of our data generation model,  
while keeping its learnable architecture constant. At the  
second level, this trained model is used to produce synthetic  
image-mask pairs, which are then employed to train a  
semantic segmentation model. The final level involves  
validating the segmentation model using real medical  
images with expert-annotated masks. The performance  
of the segmentation model in this validation phase is a  
function of the architecture of the generation model. We  
optimize this architecture by minimizing the validation loss.  
By jointly solving the three levels of nested optimization  
problems, we can concurrently train data generation and  
semantic segmentation models in an end-to-end manner.

Our framework was validated for a variety of medical  
imaging segmentation tasks across 16 datasets, spanning  
a diverse spectrum of imaging techniques, diseases, le-  
sions, and organs. These tasks comprise segmentation  
of skin lesions from dermoscopy images, breast cancer  
from ultrasound images, placental vessels from fetoscopic  
images, polyps from colonoscopy images, foot ulcers from  
standard camera images, intraretinal cystoid fluid from  
optical coherence tomography (OCT) images, lungs from  
chest X-ray images, and left ventricles and myocardial wall

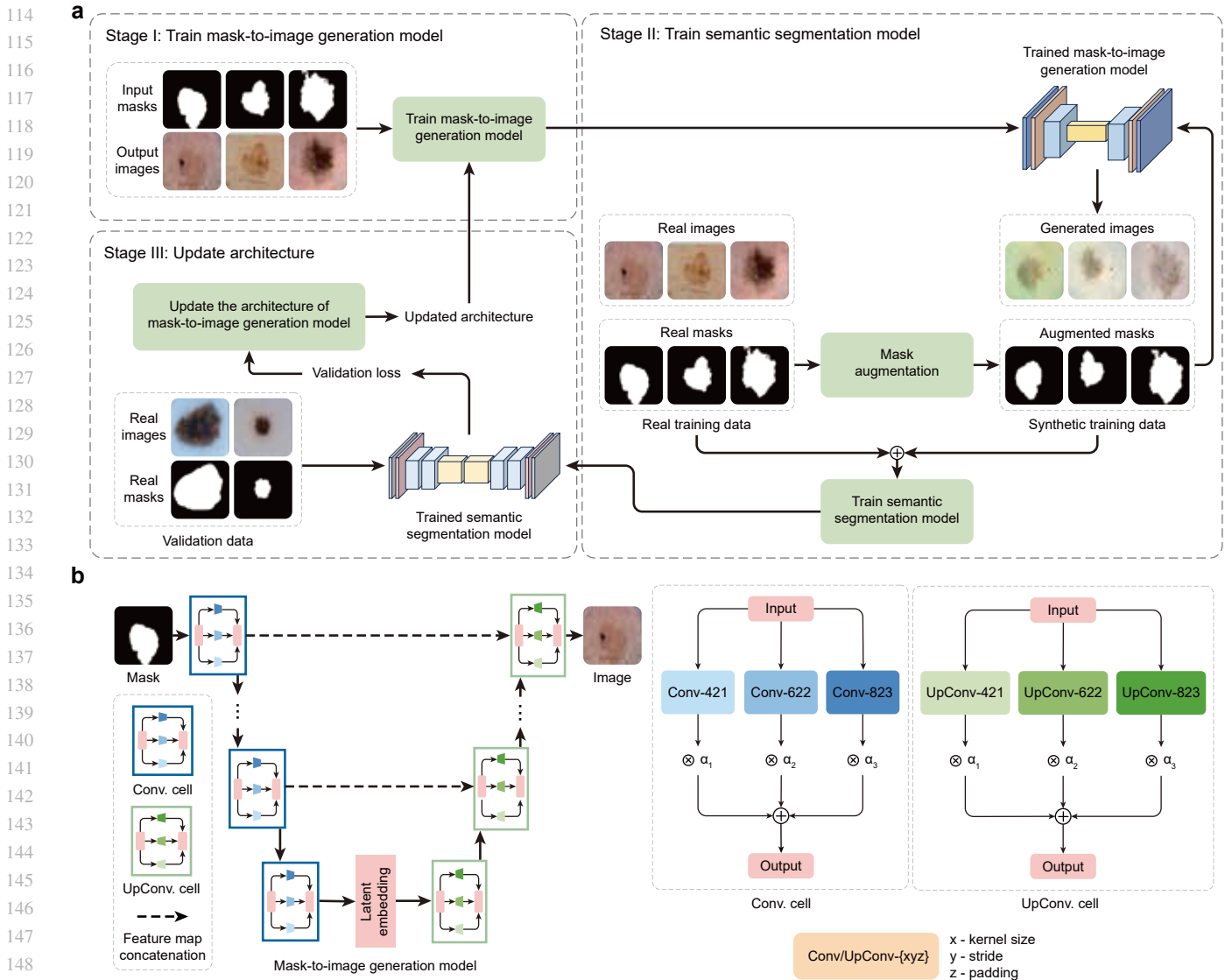


**Fig. 1 | Proposed end-to-end data generation framework for improving medical image segmentation in ultra low-data regimes.** **a**, Overview of the GenSeg framework. GenSeg consists of 1) a semantic segmentation model which takes a medical image as input and predicts a segmentation mask, and 2) a mask-to-image generation model which takes a segmentation mask as input and generates a medical image. The latter features a neural architecture that can be learned, in addition to its learnable network weights. GenSeg operates through three end-to-end learning stages. In stage I, the network weights of the mask-to-image model are trained with real mask-image pairs, while its architecture remains tentatively fixed. Stage II involves using the trained mask-to-image model to generate synthetic training data. Specifically, real segmentation masks undergo augmentation procedures to produce augmented masks which are then inputted into the mask-to-image model to generate corresponding images. These images, paired with the augmented masks, are used to train the semantic segmentation model, alongside real data. In stage III, the trained segmentation model is evaluated on a real validation dataset, and the resulting validation loss - which reflects the performance of the mask-to-image model's architecture - is used to update this architecture. Following this update, the model re-enters Stage I for further training, and this cycle continues until convergence. **b**, Searchable architecture of the mask-to-image generation model. It comprises an encoder and a decoder. The encoder processes an input mask into a latent representation using a series of searchable convolution (Conv.) cells. The decoder employs a stack of searchable up-convolution (UpConv.) cells to convert the latent representation back into an output medical image. Each cell contains multiple candidate operations characterized by varying kernel sizes, strides, and padding options. Each operation is associated with a weight  $\alpha$  denoting its importance. The process of architecture search involves optimizing these importance weights. After the learning phase, only the candidate operations with the highest weights are incorporated into the final model architecture.

from echocardiography images.

**GenSeg enables accurate segmentation in ultra low-data regimes.** We evaluated GenSeg's performance in ultra low-data regimes. Our method involved three-fold cross-validation on each dataset. GenSeg, being a versatile framework, facilitates training various backbone segmentation

models with its generated data. To demonstrate this versatility, we applied GenSeg to two popular models: UNet (25) and DeepLab (10), resulting in GenSeg-UNet and GenSeg-DeepLab, respectively. GenSeg-DeepLab and GenSeg-UNet demonstrated significant performance improvements over DeepLab and UNet in scenarios with extremely limited data (Fig. 2a and Extended Data Fig. 1b). Specifically, in the

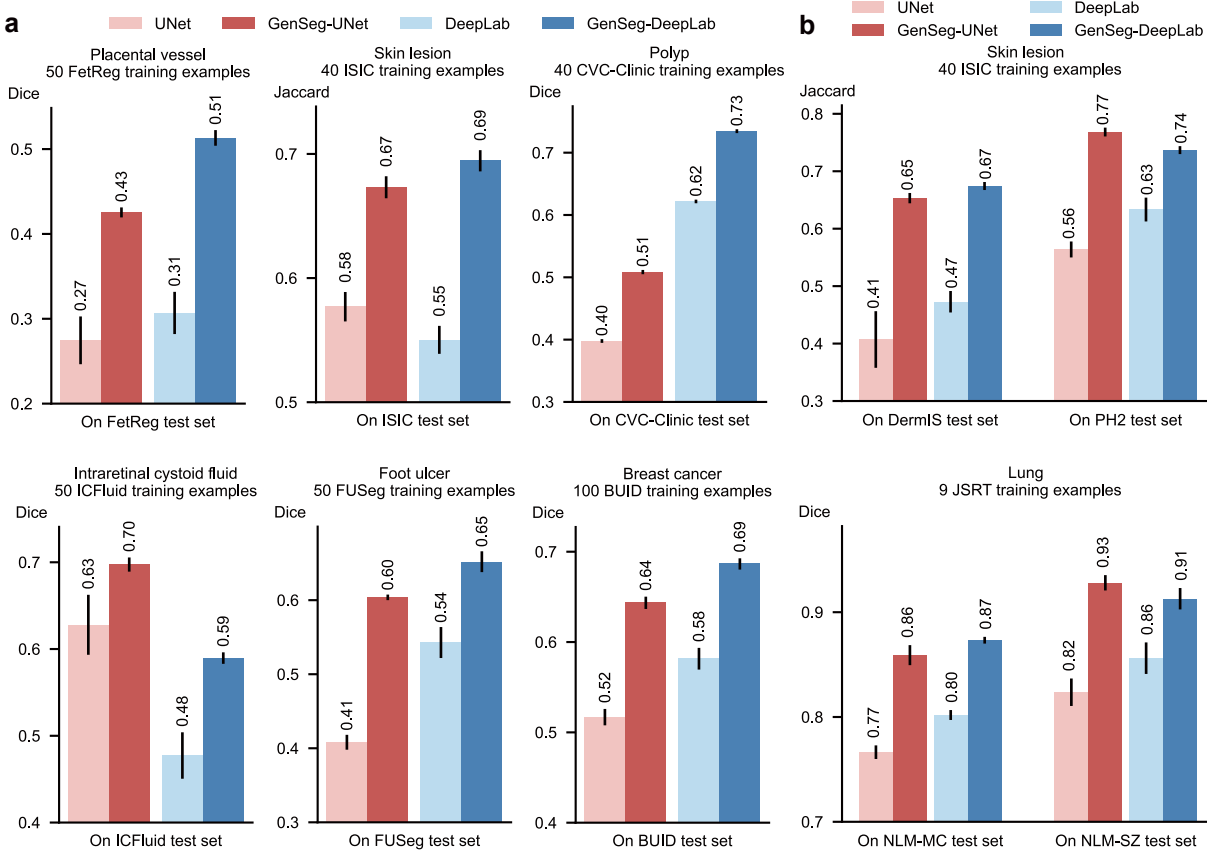


**Fig. 2 | GenSeg significantly boosted both in-domain and out-of-domain generalization performance, particularly in ultra low-data regimes.** **a**, The performance of GenSeg applied to UNet (GenSeg-UNet) and DeepLab (GenSeg-DeepLab) under in-domain settings (test and training data are from the same domain) in the tasks of segmenting placental vessels, skin lesions, polyps, intraretinal cystoid fluids, foot ulcers, and breast cancer using extremely limited training data (50, 40, 40, 50, 50, and 100 examples from the FetReg, ISIC, CVC-Clinic, ICFluid, FUSeg, and BUID datasets, respectively for each task), compared to vanilla UNet and DeepLab. **b**, The performance of GenSeg-UNet and GenSeg-DeepLab under out-of-domain settings (test and training data are from different domains) in segmenting skin lesions (using only 40 examples from the ISIC dataset for training, and the DermIS and PH2 datasets for testing) and lungs (using only 9 examples from the JSRT dataset for training, and the NLM-MC and NLM-SZ datasets for testing), compared to vanilla UNet and DeepLab.

tasks of segmenting placental vessels, skin lesions, polyps, intraretinal cystoid fluids, foot ulcers, and breast cancer, with training sets as small as 50, 40, 40, 50, 50, and 100 samples respectively, GenSeg-DeepLab outperformed DeepLab substantially, with absolute percentage gains of 20.6%, 14.5%, 11.3%, 11.3%, 10.9%, and 10.4%. Similarly, GenSeg-UNet surpassed UNet by significant margins, recording absolute percentage improvements of 15%, 9.6%, 11%, 6.9%, 19%, and 12.6% across these tasks. The extremely limited size of these training datasets presents significant challenges for accurately training DeepLab and UNet models. For example, DeepLab’s effectiveness in these tasks is limited, with performance varying from 0.31 to 0.62, averaging 0.51. In contrast, using our method, the performance significantly improves, ranging from 0.51 to 0.73 and averaging 0.64. This highlights the strong capability of our approach to achieve precise segmentation in ultra low-data regimes. Moreover, these segmentation tasks are highly diverse. For example, placental vessels involve complex branching structures, skin lesions vary in shape and size, and polyps require differen-

tiation from surrounding mucosal tissue. GenSeg demonstrated robust performance enhancements across these diverse tasks, underscoring its strong capability in achieving accurate segmentation across different diseases, organs, and imaging modalities.

**GenSeg enables robust generalization in out-of-domain settings.**

Besides in-domain evaluation where the test and training images were from disjoint subsets of the same dataset, we also evaluated GenSeg’s effectiveness in out-of-domain (OOD) scenarios, wherein the training and test images originate from distinct datasets. The OOD evaluations were also conducted in ultra low-data regimes, where the number of training examples was restricted to only 9 or 40. Our evaluations focused on two segmentation tasks: the segmentation of skin lesions from dermoscopy images and the segmentation of lungs from chest X-rays. For the task of skin lesion segmentation, we trained our models using 40 examples from the ISIC dataset. These models were then tested on two external datasets, DermIS and PH2, to evaluate their per-

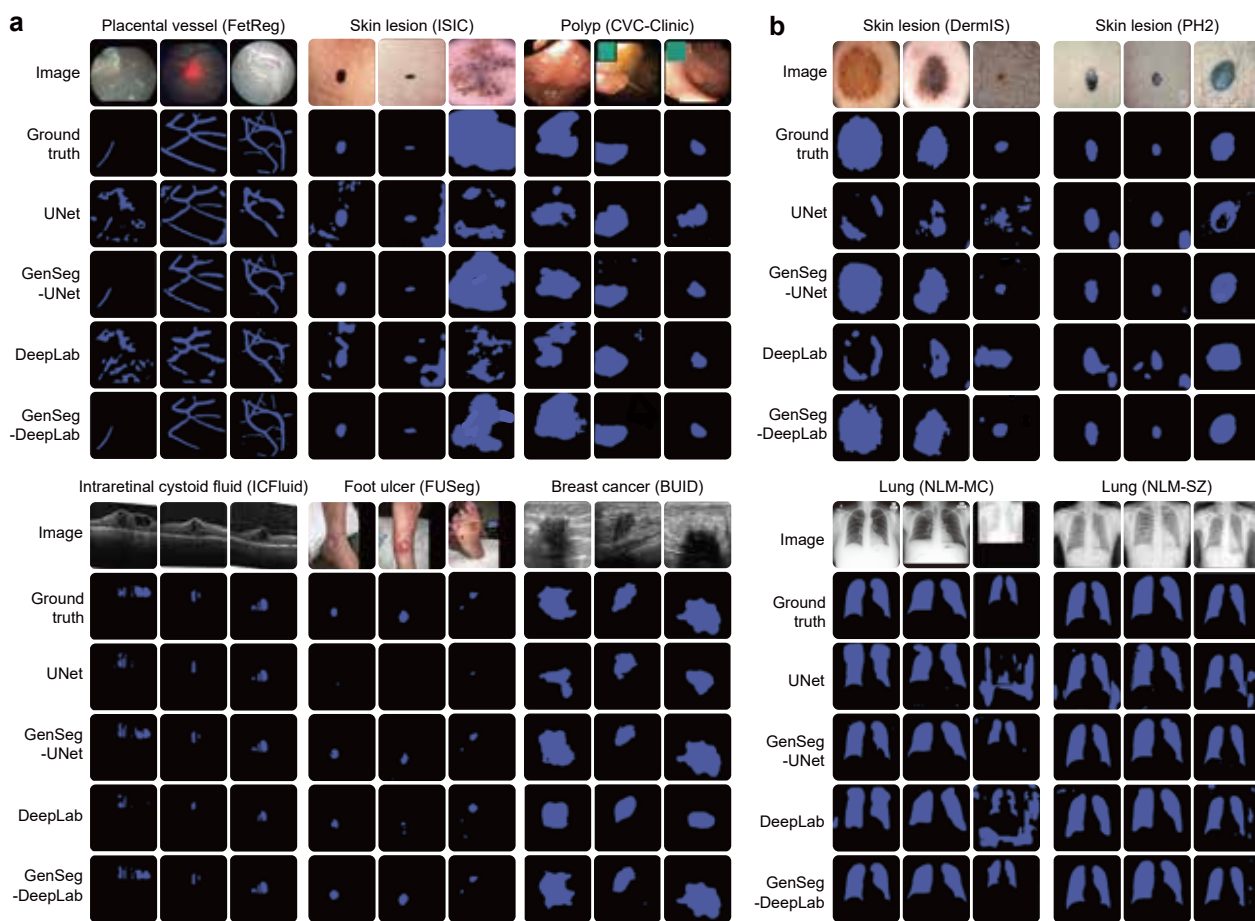


**Fig. 3 | GenSeg improves in-domain and out-of-domain generalization performance across a variety of segmentation tasks covering diverse diseases, organs, and imaging modalities.** **a**, Visualizations of segmentation masks predicted by GenSeg-DeepLab and GenSeg-UNet under in-domain settings in the tasks of segmenting placental vessels, skin lesions, polyps, intraretinal cystoid fluids, foot ulcers, and breast cancer using extremely limited training data (50, 40, 40, 50, 50, and 100 examples from the FetReg, ISIC, CVC-Clinic, ICFluid, FUSeG, and BUID datasets), compared to vanilla UNet and DeepLab. **b**, Visualizations of segmentation masks predicted by GenSeg-DeepLab and GenSeg-UNet under out-of-domain settings in segmenting skin lesions (using only 40 examples from the ISIC dataset for training, and the DermIS and PH2 datasets for testing) and lungs (using only 9 examples from the JSRT dataset for training, and the NLM-MC and NLM-SZ datasets for testing), compared to vanilla UNet and DeepLab.

formance outside the ISIC domain. In the lung segmentation task, we utilized 9 training examples from the JSRT dataset and conducted evaluations on two additional datasets, NLM-SZ and NLM-MC, to test the models' adaptability beyond the JSRT domain. GenSeg showed superior out-of-domain generalization capabilities (Fig. 2b). In skin lesion segmentation, GenSeg-UNet substantially outperformed UNet, achieving a Jaccard index of 0.65 compared to UNet's 0.41 on the DermIS dataset, and 0.77 versus 0.56 on PH2. Similarly, in lung segmentation, GenSeg-UNet demonstrated superior performance with a Dice score of 0.86 compared to UNet's 0.77 on NLM-MC, and 0.93 against 0.82 on NLM-SZ. Similarly, GenSeg-DeepLab significantly outperformed DeepLab: it achieved 0.67 compared to 0.47 on DermIS, 0.74 vs. 0.63 on PH2, 0.87 vs. 0.80 on NLM-MC, and 0.91 vs. 0.86 on NLM-SZ. Fig. 3 and Extended Data Fig. 8 visualize some randomly selected segmentation examples. Both GenSeg-UNet and GenSeg-DeepLab accurately segmented

a wide range of disease targets and organs across various imaging modalities with their predicted masks closely resembling the ground truth, under both in-domain (Fig. 3a and Extended Data Fig. 8) and out-of-domain (Fig. 3b) settings. In contrast, UNet and DeepLab struggled to achieve similar levels of accuracy, often producing masks that were less precise and exhibited inconsistencies in complex anatomical regions. This disparity underscores the advanced capabilities of GenSeg in handling varied and challenging segmentation tasks. Extended Data Fig. 9 presents several mask-image pairs generated by GenSeg. The generated images not only exhibit a high degree of realism but also demonstrate excellent semantic alignment with their corresponding masks.

**GenSeg achieves comparable performance to baselines with significantly fewer training examples.** In comparing the number of training examples required for GenSeg and baseline models to achieve similar performance,

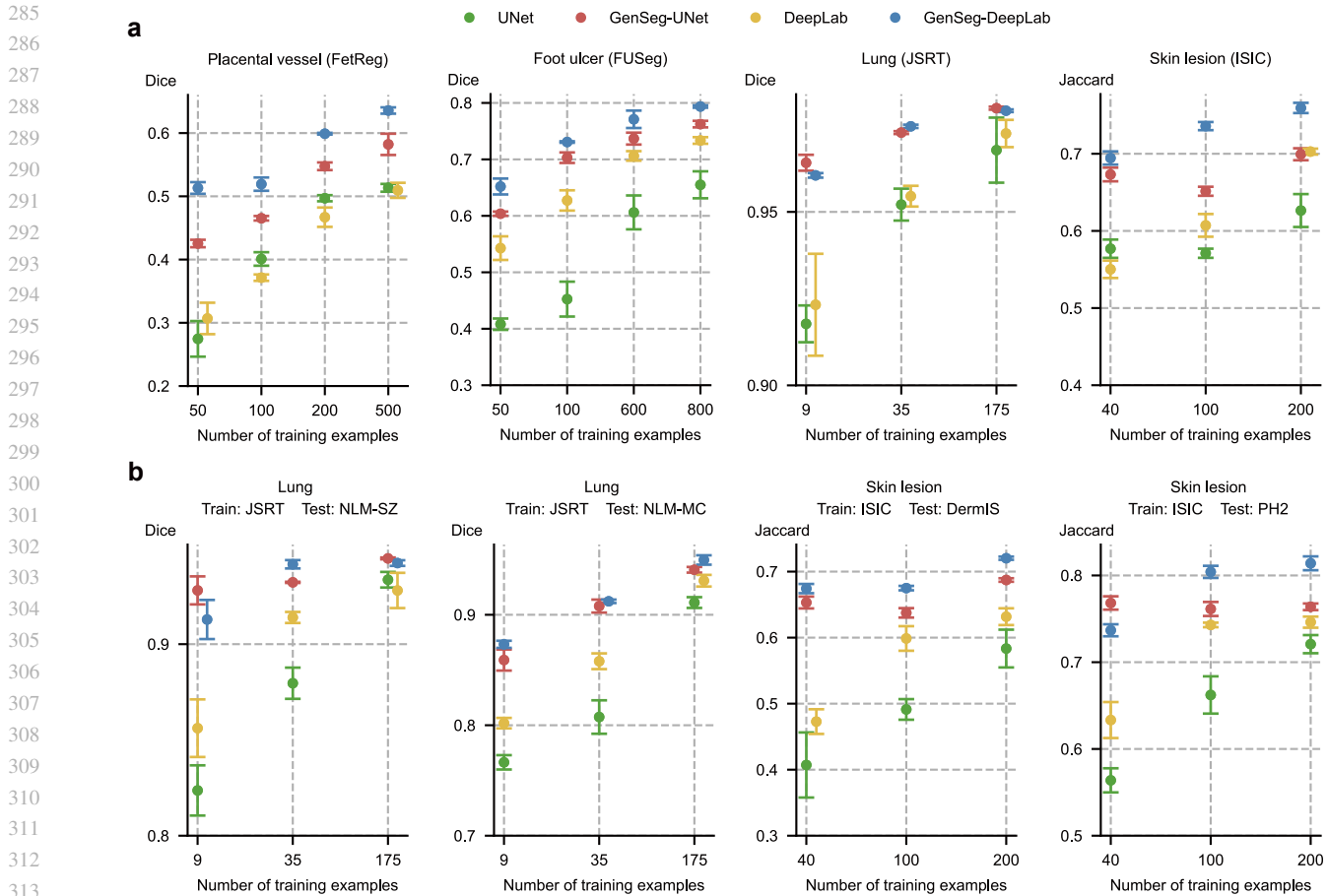


**Fig. 4 | GenSeg achieves performance on par with baseline models while requiring significantly fewer training examples.** **a**, The in-domain generalization performance of GenSeg-UNet and GenSeg-DeepLab with different numbers of training examples from the FetReg, FUSeG, JSRT, and ISIC datasets in segmenting placental vessels, foot ulcers, lungs, and skin lesions, compared to UNet and DeepLab. **b**, The out-of-domain generalization performance of GenSeg-UNet and GenSeg-DeepLab with different numbers of training examples in segmenting lungs (using examples from JSRT for training, and NLM-SZ and NLM-MC for testing) and skin lesions (using examples from ISIC for training, and DermIS and PH2 for testing), compared to UNet and DeepLab.

GenSeg consistently required fewer examples. Fig. 4 illustrates this point by plotting segmentation performance (y-axis) against the number of training examples (x-axis) for various methods. Methods that are closer to the upper left corner of the subfigure are considered more sample-efficient, as they achieve superior segmentation performance with fewer training examples. Across all subfigures, our methods consistently position nearer to these optimal upper left corners compared to the baseline methods. First, GenSeg demonstrates superior sample-efficiency under in-domain settings (Fig. 4a). For example, in the placental vessel segmentation task, GenSeg-DeepLab achieved a Dice score of 0.51 with only 50 training examples, a ten-fold reduction compared to DeepLab’s 500 examples needed to reach the same score. In foot ulcer segmentation, to reach a Dice score around 0.6, UNet needed 600 examples, in contrast to GenSeg-UNet which required only 50 examples, a twelve-fold reduction. DeepLab required 800 training examples for a Dice score of 0.73, whereas GenSeg-DeepLab achieved the same score with only 100 examples, an eight-

fold reduction. In lung segmentation, achieving a Dice score of 0.97 required 175 examples for UNet, whereas GenSeg-UNet needed just 9 examples, representing a 19-fold reduction. Second, the sample efficiency of GenSeg is also evident in out-of-domain (OOD) settings (Fig. 4b). For example, in lung segmentation, achieving an OOD generalization performance of 0.93 on the NLM-SZ dataset required 175 training examples from the JSRT dataset for UNet, while GenSeg-UNet needed only 9 examples, representing a 19-fold reduction. In skin lesion segmentation, GenSeg-DeepLab, trained with only 40 ISIC examples, reached a Jaccard index of 0.67 on DermIS, a performance that DeepLab could not match even with 200 examples.

**GenSeg outperforms widely used data augmentation and generation tools.** We compared GenSeg against prevalent data augmentation methods, including rotation, flipping, and translation, as well as their combinations. Furthermore, GenSeg was benchmarked against a data generation approach (28), which is based on the Wasserstein Generative Adversarial Network (WGAN) (29). For each baseline

342  
343  
344  
345  
346  
347  
348  
349  
350  
351  
352  
353  
354  
355  
356  
357  
358  
359  
360  
361  
362  
363  
364  
365  
366  
367  
368  
369  
370  
371  
372  
373  
374  
375  
376  
377  
378  
379  
380  
381  
382  
383  
384  
385  
386  
387  
388  
389  
390  
391  
392  
393  
394  
395  
396  
397  
398

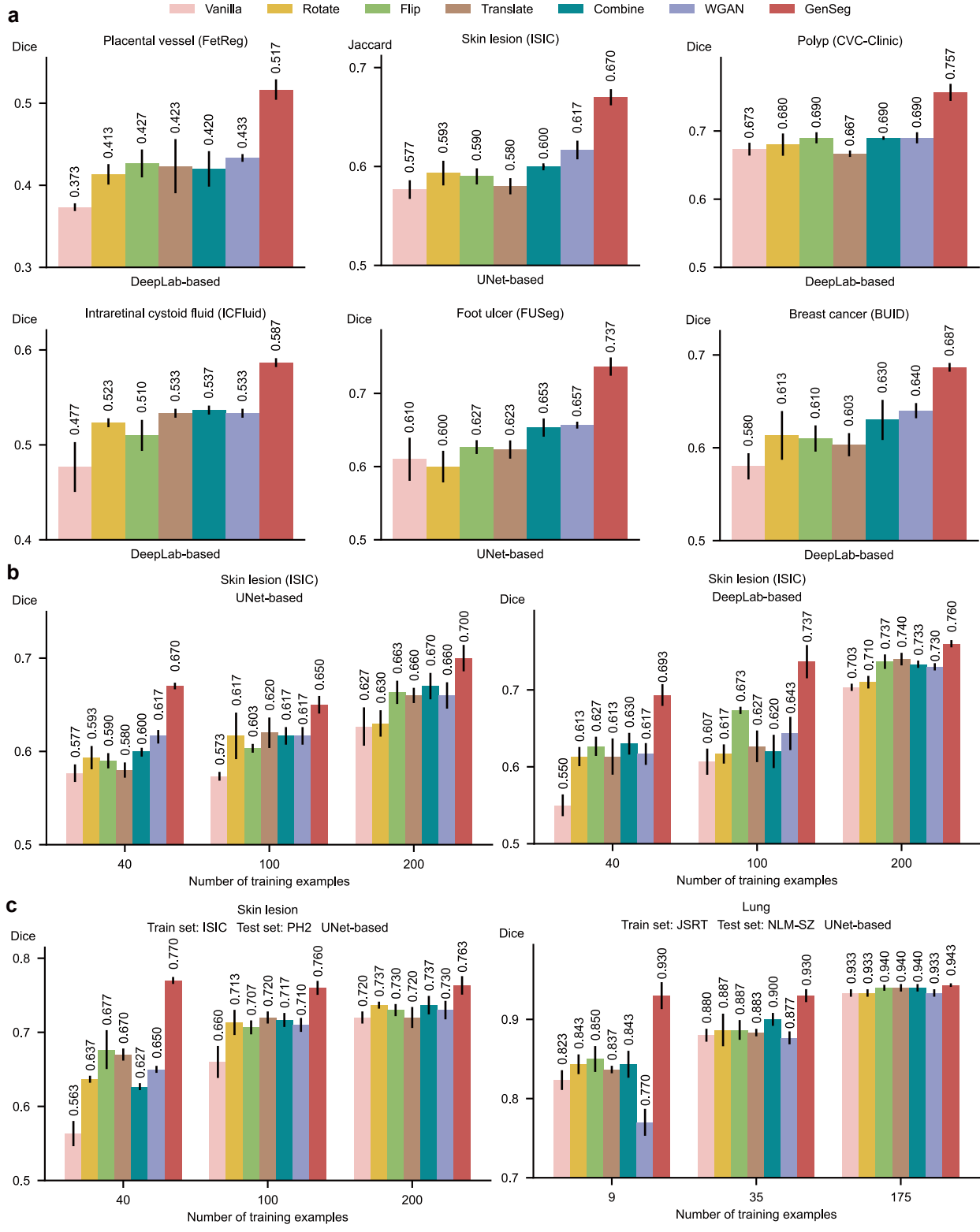


**Fig. 5 | GenSeg significantly outperformed widely used data augmentation and generation methods.** **a**, GenSeg's in-domain generalization performance compared to baseline methods including Rotate, Flip, Translate, Combine, and WGAN, when used with UNet or DeepLab in segmenting placental vessels, skin lesions, polyps, intraretinal cystoid fluids, foot ulcers, and breast cancer using the FetReg, ISIC, CVC-Clinic, ICFluid, FUSeg, and BUID datasets. **b**, GenSeg's in-domain generalization performance compared to baseline methods using a varying number of training examples from the ISIC dataset for segmenting skin lesions, with UNet and DeepLab as the backbone segmentation models. **c**, GenSeg's out-of-domain generalization performance compared to baseline methods across varying numbers of training examples in segmenting lungs (using examples from JSRT for training, and NLM-SZ and NLM-MC for testing) and skin lesions (using examples from ISIC for training, and DermIS and PH2 for testing), with UNet and DeepLab as the backbone segmentation models.

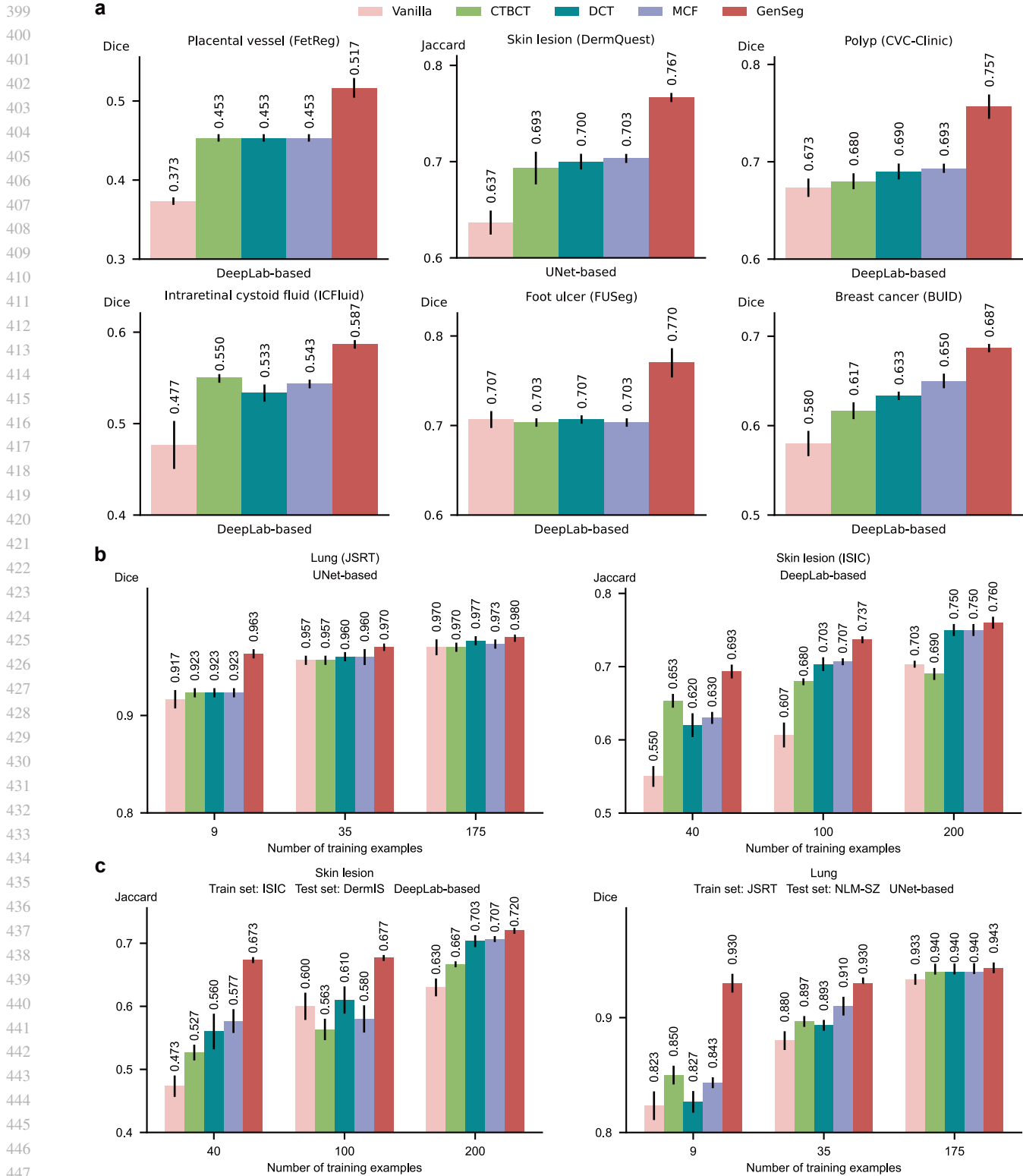


**Fig. 6 | GenSeg significantly outperformed state-of-the-art semi-supervised segmentation methods.** **a**, GenSeg's in-domain generalization performance compared to baseline methods including CTBCT, DCT, and MCF, when used with UNet or DeepLab in segmenting placental vessels, skin lesions, polyps, intraretinal cystoid fluids, foot ulcers, and breast cancer utilizing the FetReg, DermQuest, CVC-Clinic, ICFluid, FUSeg, and BUID datasets. **b**, GenSeg's in-domain generalization performance compared to baseline methods using a varying number of training examples from the ISIC and JSRT datasets for segmenting skin lesions and lungs, with UNet and DeepLab as the backbone segmentation models. **c**, GenSeg's out-of-domain generalization performance compared to baseline methods across varying numbers of training examples in segmenting lungs (using examples from JSRT for training, and NLM-SZ and NLM-MC for testing) and skin lesions (using examples from ISIC for training, and DermIS and PH2 for testing), with UNet and DeepLab as the backbone segmentation models.



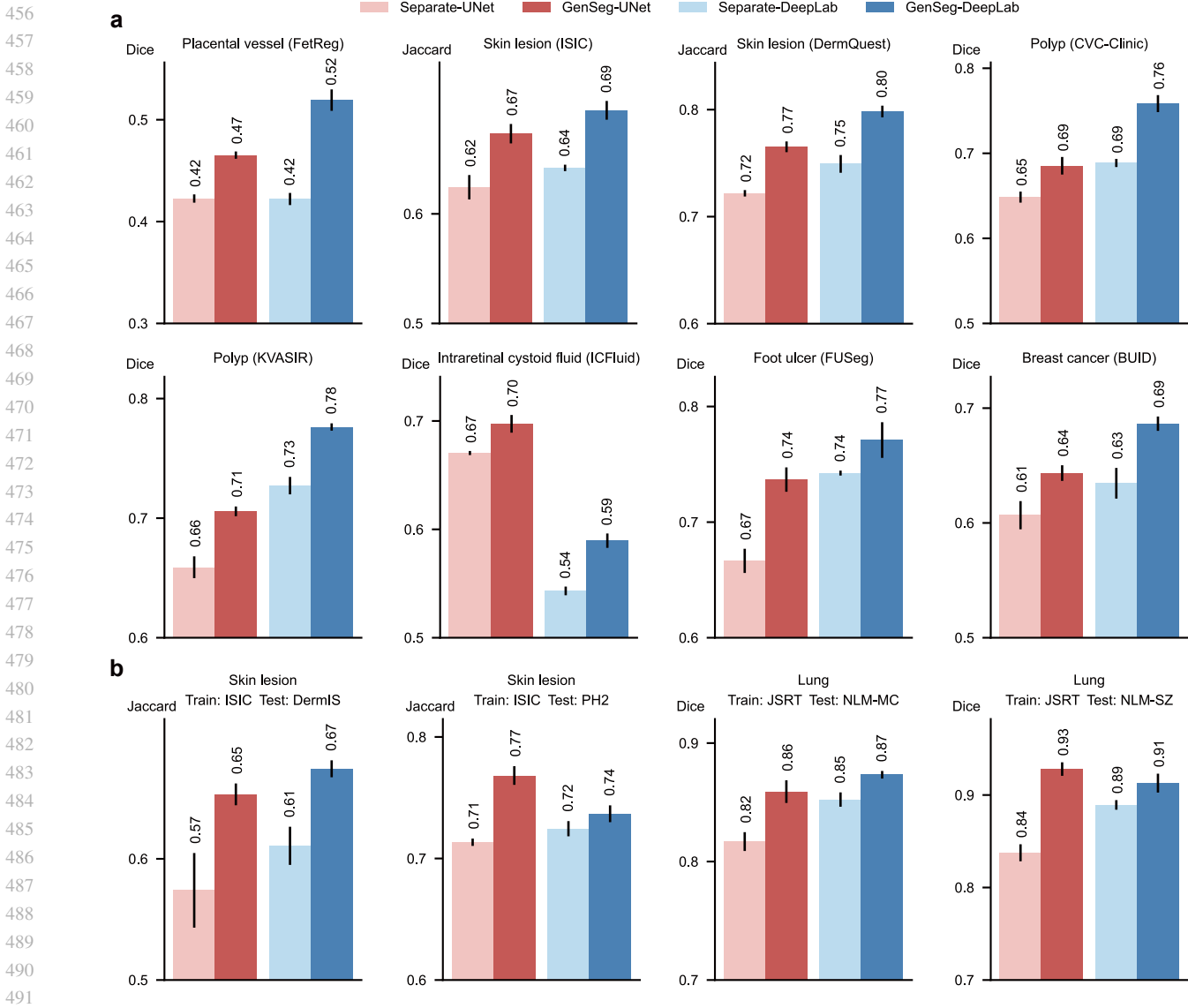


**Fig. 7 | GenSeg's end-to-end data generation mechanism significantly outperformed baselines' separate generation mechanism.** **a**, The in-domain generalization performance of GenSeg which performs data generation and segmentation model training end-to-end, compared to the Separate baseline which performs the two processes separately, when used with UNet or DeepLab in segmenting placental vessels, skin lesions, polyps, intraretinal cystoid fluids, foot ulcers, and breast cancer utilizing the FetReg, ISIC, DermQuest, CVC-Clinic, KVASIR, ICFluid, FUSeG, and BUID datasets. **b**, GenSeg's out-of-domain generalization performance compared to the Separate baseline in segmenting skin lesions (using examples from ISIC for training, and DermIS and PH2 for testing) and lungs (using examples from JSRT for training, and NLM-SZ and NLM-MC for testing), with UNet and DeepLab as the backbone segmentation models.

augmentation method, the same hyperparameters (e.g., rotation angle) were consistently applied to both the input image and the corresponding output mask within each training example, resulting in augmented image-mask pairs. GenSeg significantly surpassed these methods under in-domain settings (Fig. 5a and Extended Data Fig. 3). For instance, in foot ulcer segmentation using UNet as the backbone segmentation model, GenSeg attained a Dice score of 0.74, significantly surpassing the top baseline method, WGAN, which achieved 0.66. Similarly, in polyp segmentation with DeepLab, GenSeg scored 0.76, significantly outperforming the best baselines - Flip, Combine, and WGAN - which scored 0.69. GenSeg also demonstrated superior out-of-domain (OOD) generalization performance compared to the

baselines (Fig. 5c and Extended Data Fig. 4b). For instance, in UNet-based skin lesion segmentation, with 40 training examples from the ISIC dataset, GenSeg achieved a Dice score of 0.77 on the PH2 dataset, substantially surpassing the best-performing baseline, Flip, which scored 0.68. Moreover, GenSeg demonstrated comparable performance to baseline methods with fewer training examples (Fig. 5b and Extended Data Fig. 4a) under in-domain settings. For instance, using only 40 training examples for skin lesion segmentation with UNet, GenSeg achieved a Dice score of 0.67. In contrast, the best performing baseline, Combine, required 200 examples to reach the same score. Similarly, with fewer training examples, GenSeg achieved comparable performance to baseline methods under out-of-domain settings (Fig. 5c and Extended

513 Data Fig. 4b). For example, in lung segmentation with UNet,  
514 GenSeg reached a Dice score of 0.93 using just 9 training ex-  
515 amples, whereas the best performing baseline required 175  
516 examples to achieve a similar score.

517 **GenSeg outperforms state-of-the-art semi-supervised**  
518 **segmentation methods.** We conducted a comparative  
519 analysis of GenSeg against leading semi-supervised segmen-  
520 tation methods (18–20, 30), including cross-teaching be-  
521 tween convolutional neural networks and Transformer (CT-  
522 BCT) (31), deep co-training (DCT) (30), and a mutual cor-  
523 rection framework (MCF) (32), which employ external unlabeled  
524 images (1000 in each experiment) to enhance model  
525 training and thereby improve segmentation performance.  
526 GenSeg, which does not require any additional unlabeled  
527 images, significantly outperformed baseline methods under  
528 in-domain settings (Fig. 6a and Extended Data Fig. 5). For  
529 example, when using DeepLab as the backbone segmen-  
530 tation model for polyp segmentation, GenSeg achieved a  
531 Dice score of 0.76, markedly outperforming the top baseline  
532 method, MCF, which reached only 0.69. GenSeg also ex-  
533 hibited superior out-of-domain (OOD) generalization capa-  
534 bilities compared to baseline methods (Fig. 6c and Extended  
535 Data Fig. 6b). For instance, in skin lesion segmentation  
536 based on DeepLab with 40 training examples from the ISIC  
537 dataset, GenSeg achieved a Dice score of 0.67 on the DermIS  
538 dataset, significantly higher than the best-performing base-  
539 line, MCF, which scored 0.58. Additionally, GenSeg showed  
540 performance on par with baseline methods using fewer train-  
541 ing examples in both in-domain (Fig. 6b and Extended Data  
542 Fig. 6a) and out-of-domain settings (Fig. 6c and Extended  
543 Data Fig. 6b).

544 **GenSeg’s end-to-end generation mechanism is supe-**  
545 **rior to baselines’ separate generation.** We compared the  
546 effectiveness of GenSeg’s end-to-end data generation mech-  
547 anism against a baseline approach, Separate, which separates  
548 data generation from segmentation model training. In Sepa-  
549 rate, the mask-to-image generation model is initially trained  
550 and then fixed. Subsequently, it generates data, which is then  
551 utilized to train the segmentation model. The end-to-end  
552 GenSeg framework consistently outperformed the Separate  
553 approach under both in-domain (Fig. 7a and Extended Data  
554 Fig. 7a) and out-of-domain settings (Fig. 7b and Extended  
555 Data Fig. 7b). For instance, in the segmentation of placental  
556 vessels, GenSeg-DeepLab attained an in-domain Dice score  
557 of 0.52, significantly surpassing Separate-DeepLab, which  
558 scored 0.42. In lung segmentation using JSRT as the train-  
559 ing dataset, GenSeg-UNet achieved an out-of-domain Dice  
560 score of 0.93 on the NLM-SZ dataset, considerably better  
561 than the 0.84 scored by Separate-UNet.

562 **GenSeg improves the performance of diverse back-**  
563 **bone segmentation models.** GenSeg is a versatile,  
564 model-agnostic framework that can seamlessly integrate  
565 with segmentation models with diverse architectures to im-  
566 prove their performance. After applying our framework

on U-Net and DeepLab, we observed significant enhance-  
ments in their performance (Figs. 2–7), both for in-domain  
and out-of-domain settings. Furthermore, we also inte-  
grated this framework with a Transformer-based segmen-  
tation model, SwinUnet (33). Using just 40 training examples  
from the ISIC dataset, GenSeg-SwinUnet achieved a Jaccard  
index of 0.62 on the ISIC test set. Furthermore, it demon-  
strated strong generalization with out-of-domain Jaccard in-  
dex scores of 0.65 on the PH2 dataset and 0.62 on the DermIS  
dataset. These results represent a substantial improve-  
ment over the baseline SwinUnet model, which achieved  
Jaccard indices of 0.55 on ISIC, 0.56 on PH2, and 0.38 on  
DermIS (Extended Data Fig. 1a).

## Discussion

We present GenSeg, a generative deep learning framework  
designed for generating high-quality training data to en-  
hance the training of medical image segmentation models.  
Demonstrating superior performance across eight diverse  
segmentation tasks and 17 datasets, GenSeg excels particu-  
larly in scenarios with an extremely limited number of real,  
expert-annotated training examples (as few as 50). This ultra  
low-data regime often hinders the training of effective and  
broadly applicable segmentation models, especially those  
with hundreds of millions of parameters. GenSeg effectively  
overcomes this challenge by supplementing the training  
process with its generated high-fidelity data examples.

GenSeg stands out by requiring fewer expert-annotated  
real training examples compared to baseline methods,  
yet it achieves comparable performance. This substantial  
reduction in the need for manually labeled segmentation  
masks significantly cuts down both the burden and costs  
associated with medical image annotation. With just a  
small set of real examples, GenSeg effectively trains a data  
generation model which then produces additional synthetic  
data, effectively mimicking the benefits of using a large  
dataset of real examples.

GenSeg significantly improves segmentation models’  
out-of-domain (OOD) generalization capability. GenSeg is  
capable of generating diverse medical images accompanied  
by precise segmentation masks. When trained on this  
diverse augmented dataset, segmentation models can learn  
more robust and OOD generalizable feature representations.

GenSeg stands out from current data augmentation and  
generation techniques by offering superior segmentation  
performance, primarily due to its end-to-end data generation  
mechanism. Unlike previous methods that separate data  
augmentation/generation and segmentation model training,  
our approach integrates them end-to-end within a unified,  
multi-level optimization framework. Within this framework,  
the validation performance of the segmentation model acts  
as a direct indicator of the generated data’s usefulness. By  
leveraging this performance to inform the training process

of the generation model, we ensure that the data produced is specifically optimized to improve the segmentation model. In previous methods, segmentation performance does not impact the process of data augmentation and generation. As a result, the augmented/generated data might not be effectively tailored for training the segmentation model. Furthermore, our framework learns a generative model that excels in generating data with greater diversity compared to existing augmentation methods.

GenSeg excels in surpassing semi-supervised segmentation methods without the need for external unlabeled images. In the context of medical imaging, collecting even unlabeled images presents a significant challenge due to stringent privacy concerns and regulatory constraints (e.g., IRB approval), thereby reducing the feasibility of semi-supervised methods. Despite the use of unlabeled real images, semi-supervised approaches underperform compared to GenSeg. This is primarily because these methods struggle to generate accurate masks for unlabeled images, meaning they are less effective at creating labeled training data. On the other hand, GenSeg is capable of producing high-quality images from masks, ensuring a close correspondence between the images' content and the masks, thereby efficiently generating labeled training examples.

Our framework is designed to be universally applicable and independent of specific models. This design enables it to augment the capabilities of a broad spectrum of semantic segmentation models. To apply our framework to a specific segmentation model, the only requirement is to integrate the segmentation model into the second and third stages of our framework. This straightforward process enables researchers and practitioners to easily utilize our approach to improve the performance of diverse semantic segmentation models.

In summary, GenSeg is a robust data generation tool that seamlessly integrates with current semantic segmentation models. It significantly enhances both in-domain and out-of-domain generalization performance in ultra low-data regimes, markedly boosting sample efficiency. Furthermore, it surpasses state-of-the-art methods in data augmentation and semi-supervised learning.

## References

1. Olaf Ronneberger, Philipp Fischer, and Thomas Brox. U-net: Convolutional networks for biomedical image segmentation. In *Medical Image Computing and Computer-Assisted Intervention—MICCAI: 18th International Conference*, pages 234–241. Springer, 2015.
2. Fabian Isensee, Paul F Jaeger, Simon AA Kohl, Jens Petersen, and Klaus H Maier-Hein. nnu-net: a self-configuring method for deep learning-based biomedical image segmentation. *Nature methods*, 18(2):203–211, 2021.
3. Jun Ma, Yuting He, Feifei Li, Lin Han, Chenyu You, and Bo Wang. Segment anything in medical images. *Nature Communications*, 15(1):654, 2024.
4. Michela Antonelli, Annika Reinke, Spyridon Bakas, Keyvan Farahani, Annette Kopp-Schneider, Bennett A Landman, Geert Litjens, Bjoern Menze, Olaf Ronneberger, Ronald M Summers, et al. The medical segmentation decathlon. *Nature communications*, 13(1): 4128, 2022.
5. Jiantao Pu, Joseph K Leader, Andriy Bandos, Shi Ke, Jing Wang, Junli Shi, Pang Du, Youmin Guo, Sally E Wenzel, Carl R Fuhrman, et al. Automated quantification of covid-19 severity and progression using chest ct images. *European radiology*, 31:436–446, 2021.
6. Habib Zaidi and Issam El Naqa. Pet-guided delineation of radiation therapy treatment volumes: a survey of image segmentation techniques. *European journal of nuclear medicine and molecular imaging*, 37:2165–2187, 2010.
7. Maria Grammatikopoulou, Evangello Flouty, Abdolrahim Kadkhodamohammadi, Gwenolé Quellec, Andre Chow, Jean Nehme, Imanol Luengo, and Danail Stoyanov. Cadis: Cataract dataset for surgical rgb-image segmentation. *Medical Image Analysis*, 71:102053, 2021.
8. Himashi Peiris, Munawar Hayat, Zhaolin Chen, Gary Egan, and Mehrtaash Harandi. Uncertainty-guided dual-views for semi-supervised volumetric medical image segmentation. *Nature Machine Intelligence*, 5(7):724–738, 2023.
9. Shanshan Wang, Cheng Li, Rongpin Wang, Zaiyi Liu, Meiyun Wang, Hongna Tan, Yaping Wu, Xinfeng Liu, Hui Sun, Rui Yang, et al. Annotation-efficient deep learning for automatic medical image segmentation. *Nature communications*, 12(1):5915, 2021.
10. Liang-Chieh Chen, George Papandreou, Iasonas Kokkinos, Kevin Murphy, and Alan L Yuille. Deeplab: Semantic image segmentation with deep convolutional nets, atrous convolution, and fully connected crfs. *IEEE transactions on pattern analysis and machine intelligence*, 40(4):834–848, 2017.
11. Enze Xie, Wenhai Wang, Zhiding Yu, Anima Anandkumar, Jose M Alvarez, and Ping Luo. Segformer: Simple and efficient design for semantic segmentation with transformers. *Advances in neural information processing systems*, 34:12077–12090, 2021.
12. Raphael Schäfer, Till Nicke, Henning Höfener, Annkristin Lange, Dorit Merhof, Friedrich Feuerhake, Volkmar Schulz, Johannes Lotz, and Fabian Kiessling. Overcoming data scarcity in biomedical imaging with a foundational multi-task model. *Nature Computational Science*, pages 1–15, 2024.
13. Yuhua Chen, Wen Li, Xiaoran Chen, and Luc Van Gool. Learning semantic segmentation from synthetic data: A geometrically guided input-output adaptation approach. In *Proceedings of the IEEE/CVF conference on computer vision and pattern recognition*, pages 1841–1850, 2019.
14. Jaehoon Choi, Taekyung Kim, and Changick Kim. Self-ensembling with gan-based data augmentation for domain adaptation in semantic segmentation. In *Proceedings of the IEEE/CVF International Conference on Computer Vision*, pages 6830–6840, 2019.
15. Veit Sandfort, Ke Yan, Perry J Pickhardt, and Ronald M Summers. Data augmentation using generative adversarial networks (cyclegan) to improve generalizability in ct segmentation tasks. *Scientific reports*, 9(1):16884, 2019.
16. Quang Nguyen, Truong Vu, Anh Tran, and Khoi Nguyen. Dataset diffusion: Diffusion-based synthetic data generation for pixel-level semantic segmentation. *Advances in Neural Information Processing Systems*, 36, 2024.
17. Yassine Ouali, Céline Hudelot, and Myriam Tami. Semi-supervised semantic segmentation with cross-consistency training. In *Proceedings of the IEEE/CVF conference on computer vision and pattern recognition*, pages 12674–12684, 2020.
18. Robert Mendel, Luis Antonio De Souza, David Rauber, Joao Paulo Papa, and Christoph Palm. Semi-supervised segmentation based on error-correcting supervision. In *Proceedings of the European Conference on Computer Vision*, pages 141–157. Springer, 2020.
19. Xiaokang Chen, Yuhui Yuan, Gang Zeng, and Jingdong Wang. Semi-supervised semantic segmentation with cross pseudo supervision. In *Proceedings of the IEEE/CVF conference on computer vision and pattern recognition*, pages 2613–2622, 2021.
20. Daqing Li, Junlin Yang, Karsten Kreis, Antonio Torralba, and Sanja Fidler. Semantic segmentation with generative models: Semi-supervised learning and strong out-of-domain generalization. In *Proceedings of the IEEE/CVF conference on computer vision and pattern recognition*, pages 8300–8311, 2021.
21. A Jo. The promise and peril of generative ai. *Nature*, 614(1):214–216, 2023.
22. Ian Goodfellow, Jean Pouget-Abadie, Mehdi Mirza, Bing Xu, David Warde-Farley, Sherjil Ozair, Aaron Courville, and Yoshua Bengio. Generative adversarial nets. *Advances in neural information processing systems*, 27, 2014.
23. Jonathan Ho, Ajay Jain, and Pieter Abbeel. Denoising diffusion probabilistic models. *Advances in neural information processing systems*, 33:6840–6851, 2020.
24. Sang Keun Choe, Willie Neiswanger, Pengtao Xie, and Eric Xing. Betty: An automatic differentiation library for multilevel optimization. In *The Eleventh International Conference on Learning Representations*, 2023.
25. Olaf Ronneberger, Philipp Fischer, and Thomas Brox. U-net: Convolutional networks for biomedical image segmentation. In *Medical Image Computing and Computer-Assisted Intervention (MICCAI)*, volume 9351, pages 234–241. Springer, Cham, 2015. doi: 10.1007/978-3-319-24574-4\_28.
26. Andrew Brock, Jeff Donahue, and Karen Simonyan. Large scale gan training for high fidelity natural image synthesis. In *International Conference on Learning Representations*, 2018.
27. Yang Song, Jascha Sohl-Dickstein, Diederik P Kingma, Abhishek Kumar, Stefano Ermon, and Ben Poole. Score-based generative modeling through stochastic differential equations. *International Conference on Learning Representations*, 2021.
28. Thomas Neff, Christian Payer, Darko Štern, and Martin Urschler. Generative adversarial networks to synthetically augment data for deep learning based image segmentation. In *Proceedings of the OAGM Workshop*, pages 22–29, 2018.
29. Martin Arjovsky, Soumith Chintala, and Léon Bottou. Wasserstein generative adversarial networks. In *International conference on machine learning*, pages 214–223. PMLR, 2017.
30. Jizong Peng, Guillermo Estrada, Marco Pedersoli, and Christian Desrosiers. Deep co-training for semi-supervised image segmentation. *Pattern Recognition*, 107:107269, 2020.
31. Xiangde Luo, Minhao Hu, Tao Song, Guotai Wang, and Shaoting Zhang. Semi-supervised medical image segmentation via cross teaching between cnn and transformer. In *International Conference on Medical Imaging with Deep Learning*, pages 820–833. PMLR, 2022.
32. Yongchao Wang, Bin Xiao, Xiuli Bi, Weisheng Li, and Xinbo Gao. Mcf: Mutual correction framework for semi-supervised medical image segmentation. In *Proceedings of the IEEE/CVF conference on computer vision and pattern recognition*, pages 15651–15660, 2023.

627 33. Hu Cao, Yueyue Wang, Joy Chen, Dongsheng Jiang, Xiaopeng Zhang, Qi Tian, and Man-  
628 ning Wang. Swin-unet: Unet-like pure transformer for medical image segmentation. In  
629 *Proceedings of the European Conference on Computer Vision*, pages 205–218. Springer,  
630 2022.

## 631 Methods

632 **Overview of GenSeg.** GenSeg consists of a data gen-  
633 eration model and a medical image segmentation model.  
634 The data generation model is based on conditional gener-  
635 ative adversarial networks (GANs) (34, 35). It comprises  
636 two main components: a mask-to-image generator and  
637 a discriminator. Uniquely, our generator has a learnable  
638 neural architecture (36), as opposed to the fixed architecture  
639 commonly seen in previous GAN models. This generator,  
640 with weight parameters  $G$  and a learnable architecture  
641  $A$ , takes a segmentation mask as input and generates a  
642 corresponding medical image. The discriminator, with  
643 learnable weight parameters  $H$  and a fixed architecture,  
644 differentiates between synthetic and real medical images.  
645 The segmentation model has learnable weight parameters  $S$   
646 and a fixed architecture.

647 Data generation is executed in a reverse manner. Starting  
648 with an expert-annotated segmentation mask  $M$ , we first  
649 apply basic image augmentations, such as rotation, flipping,  
650 etc., to produce an augmented mask  $\widehat{M}$ . This mask is then  
651 fed into the mask-to-image generator, resulting in a medical  
652 image  $\hat{I}(\widehat{M}, G, A)$ , which corresponds to  $\widehat{M}$ , i.e., pixels in  
653  $\hat{I}(\widehat{M}, G, A)$  can be semantically labeled using  $\widehat{M}$ . Each  
654 image-mask pair  $(\hat{I}(\widehat{M}, G, A), \widehat{M})$  forms an augmented  
655 example for training the segmentation model. Like other  
656 deep learning-based segmentation methods, GenSeg has  
657 access to a training set comprised of real image-mask  
658 pairs  $D_{seg}^{tr} = \{I_n^{(tr)}, M_n^{(tr)}\}_{n=1}^{N_{tr}}$  and a validation set  
659  $D_{seg}^{val} = \{I_n^{(val)}, M_n^{(val)}\}_{n=1}^{N_{val}}$ .

### 660 A multi-level optimization framework for GenSeg.

661 GenSeg employs a multi-level optimization strategy across  
662 three distinct stages. The initial stage focuses on training  
663 the data generation model, where we fix the generator’s  
664 architecture  $A$  and train the weight parameters of both the  
665 generator ( $G$ ) and the discriminator ( $H$ ). To facilitate this  
666 training, we modify the segmentation training dataset  $D_{seg}^{tr}$   
667 by swapping the roles of inputs and outputs, resulting in  
668 a new dataset  $D_{gan} = \{M_n^{(tr)}, I_n^{(tr)}\}_{n=1}^{N_{tr}}$ . In this setup,  
669  $M_n^{(tr)}$  serves as the input, while  $I_n^{(tr)}$  acts as the output for  
670 our mask-to-image GAN model.

671 Let  $L_{gan}$  represent the GAN training objective, a cross-  
672 entropy function that evaluates the discriminator’s ability  
673 to distinguish between real and generated images. The  
674 discriminator’s goal is to maximize  $L_{gan}$ , effectively  
675 separating real images from generated ones. Conversely,  
676 the generator strives to minimize  $L_{gan}$ , generating images  
677 that are so realistic they become indistinguishable from real  
678 ones.

679 This process is encapsulated in the following minimax  
680 optimization problem:

$$G^*(A), H^* = \underset{G}{\operatorname{argmin}} \underset{H}{\operatorname{argmax}} L_{gan}(G, A, H, D_{gan}), \quad (1)$$

681 where  $G^*(A)$  indicates that the optimally trained generator  
682  $G^*$  is dependent on the architecture  $A$ . This dependency  
683 arises because  $G^*$  is the outcome of optimizing the training  
684 objective function, which in turn is influenced by  $A$ .  $A$   
685 is tentatively fixed at this stage and will be updated later.  
686 Otherwise, if we learn  $A$  by minimizing the training loss  
687  $L_{gan}$ , it may lead to a trivial solution characterized by an  
688 overly large and complex  $A$ . Such a solution would likely  
689 fit the training data perfectly but perform inadequately on  
690 unseen test data due to overfitting.

691 In the second stage, we leverage the trained generator  
692 to generate synthetic training examples using the afore-  
693 mentioned process where expert-annotated masks are from  
694  $D_{seg}^{tr}$ . Let  $\widehat{D}(G^*(A), D_{seg}^{tr})$  represent the generated data.  
695 We then use  $\widehat{D}(G^*(A), D_{seg}^{tr})$  and real training data  $D_{seg}^{tr}$   
696 to train the segmentation model  $S$  by minimizing a segmen-  
697 tation loss  $L_{seg}$  (pixel-wise cross-entropy loss). This training  
698 is formulated as the following optimization problem:

$$S^*(A) = \underset{S}{\operatorname{argmin}} L_{seg}(S, \widehat{D}(G^*(A), D_{seg}^{tr})) + \gamma L_{seg}(S, D_{seg}^{tr}), \quad (2)$$

699 where  $\gamma$  is a trade-off parameter.

700 In the third stage, we assess the performance of the  
701 trained segmentation model on the validation dataset  $D_{seg}^{val}$ .  
702 The validation loss,  $L_{seg}(S^*(A), D_{seg}^{val})$ , serves as an indi-  
703 cator of the quality of the generated data. If the generated  
704 data is of inferior quality, it will likely result in  $S^*(A)$  -  
705 trained on this data - performing poorly on the validation  
706 set, reflected in a high validation loss. Thus, enhancing the  
707 quality of generated data can be achieved by minimizing  
708  $L_{seg}(S^*(A), D_{seg}^{val})$  w.r.t the generator’s architecture  $A$ .  
709 This objective is encapsulated in the following optimization  
710 problem:

$$\min_A L_{seg}(S^*(A), D_{seg}^{val}). \quad (3)$$

711 We can integrate these stages into a multi-level optimization  
712 problem as follows:

$$\begin{aligned} \min_A \quad & L_{seg}(S^*(A), D_{seg}^{val}) \\ \text{s.t.} \quad & S^*(A) = \underset{S}{\operatorname{argmin}} L_{seg}(S, \widehat{D}(G^*(A), D_{seg}^{tr})) + \\ & \gamma L_{seg}(S, D_{seg}^{tr}) \\ & G^*(A), H^* = \underset{G}{\operatorname{argmin}} \underset{H}{\operatorname{argmax}} L_{gan}(G, A, H, D_{gan}) \end{aligned} \quad (4)$$

713 In this formulation, the levels are interdependent. The out-  
714 put  $G^*(A)$  from the first level defines the objective for the  
715 second level, the output  $S^*(A)$  from the second level defines  
716 the objective for the third level, and the optimization variable  
717  $A$  in the third level defines the objective function in the first  
718 level.

684 **Architecture search space.** To enhance the generation  
685 of medical images by accurately capturing their distinctive  
686 characteristics, we make the generator’s architecture search-  
687 able. Inspired by DARTS (37), we employ a differentiable  
688 search method that is not only computationally efficient but  
689 also allows for a flexible exploration of architectural de-  
690 signs. Our search space is structured as a series of compu-  
691 tational cells, each forming a directed acyclic graph that  
692 includes an input node, an output node, and intermediate  
693 nodes comprising  $K$  different operators, such as convolu-  
694 tion and transposed convolution. These operators are each  
695 tied to a learnable selection weight,  $\alpha$ , ranging from 0 to 1,  
696 where a higher  $\alpha$  value indicates a stronger preference for  
697 incorporating that operator into the final architecture. The  
698 process of architecture search is essentially the optimization  
699 of these selection weights. Let  $\text{Conv-}xyz$  and  $\text{UpConv-}xyz$   
700 denote a convolution operator and a transposed convolution  
701 operator respectively, where  $x$  represents the kernel size,  $y$   
702 the stride, and  $z$  the padding. The pool of candidate oper-  
703 ators includes  $\text{Conv/UpConv-421}$ ,  $\text{Conv/UpConv-622}$ , and  
704  $\text{Conv/UpConv-823}$ , i.e., the number of operators  $K$  is 3. For  
705 any given cell  $i$  with input  $x_i$ , the output  $y_i$  is determined  
706 by the formula  $y_i = \sum_{k=1}^K \alpha_{i,k} \mathbf{o}_{i,k}(x_i)$ , where  $\mathbf{o}_{i,k}$  repre-  
707 sents the  $k$ -th operator in the cell, and  $\alpha_{i,k}$  is its correspond-  
708 ing selection weight. Consequently, the architecture of the  
709 generator can be succinctly described by the set of all selec-  
710 tion weights, denoted as  $A = \{\alpha_{i,k}\}$ . Architecture search  
711 amounts to learning  $A$ .

712  
713 **Optimization algorithm.** We develop a gradient-based  
714 method to solve the multi-level optimization problem in  
715 Eq.(4). First, we approximate  $G^*(A)$  using one-step gra-  
716 dient descent update of  $G$  w.r.t  $L_{gan}(G, A, H, D_{gan})$ :

$$717 \quad G^*(A) \approx G' = G - \eta_g \nabla_G L_{gan}(G, A, H, D_{gan}), \quad (5)$$

718 where  $\eta_g$  is a learning rate. Similarly, we approxi-  
719 mate  $H^*$  using one-step gradient ascent update of  $H$  w.r.t  
720  $L_{gan}(G, A, H, D_{gan})$ :

$$721 \quad H^* \approx H' = H + \eta_h \nabla_H L_{gan}(G, A, H, D_{gan}). \quad (6)$$

722  
723 Then we plug  $G^*(A) \approx G'$  into the objective function in the  
724 second level, yielding an approximated objective. We ap-  
725 proximate  $S^*(A)$  using one-step gradient ascent update of  $S$   
726 w.r.t the approximated objective:

$$727 \quad S^*(A) \approx S' = S - \eta_s \nabla_S (L_{seg}(S, \hat{D}(G', D_{seg}^{tr})) + \gamma L_{seg}(S, D_{seg}^{tr})). \quad (7)$$

728  
729 Finally, we plug  $S^*(A) \approx S'$  into the validation loss in the  
730 third level, yielding an approximated validation loss. We up-  
731 date  $A$  using gradient descent w.r.t the approximated loss:

$$732 \quad A \leftarrow A - \eta_a \nabla_A L_{seg}(S', D_{seg}^{val}). \quad (8)$$

733  
734 After  $A$  is updated, we plug it into Eq.(5) to update  $G$  again.  
735 The update steps in Eq.(5-8) iterate until convergence.

Task	Dataset	Train	Validate	Test
Skin lesion segmentation	ISIC	160	40	594
	PH2	-	-	200
	DermIS	-	-	98
	DermQuest	32	8	61
Lung segmentation	JSRT	140	35	72
	NLM-MC	-	-	138
	NLM-SZ	-	-	566
Breast cancer segmentation	COVID	8	2	583
	BUID	80	20	230
Placental vessel segmentation	FPD	80	20	182
	FetReg	80	20	658
Polyp segmentation	KVASIR	480	120	200
	CVC-Clinic	80	20	212
Foot ulcer segmentation	FUSeg	480	120	200
Intraretinal cystoid segmentation	ICFluid	40	10	460
Left ventricle segmentation	ETAB (Left ventricle)	8	2	50
Myocardial wall segmentation	ETAB (Myocardial wall)	8	2	50

Table 1. Dataset statistics.

The gradient  $\nabla_A L_{seg}(S', D_{seg}^{val})$  can be calculated as follows:

$$\nabla_A L_{seg}(S', D_{seg}^{val}) = \frac{\partial G'}{\partial A} \frac{\partial S'}{\partial G'} \frac{\partial L_{seg}(S', D_{seg}^{val})}{\partial S'}, \quad (9)$$

where

$$\frac{\partial G'}{\partial A} = -\eta_g \nabla_{A,G}^2 L_{gan}(G, A, H, D_{gan}), \quad (10)$$

$$\frac{\partial S'}{\partial G'} = -\eta_s \nabla_{G',S}^2 (L_{seg}(S, \hat{D}(G', D_{seg}^{tr})) + \gamma L_{seg}(S, D_{seg}^{tr})). \quad (11)$$

**Datasets.** In this study, we focused on the segmentation of skin lesions from dermoscopy images, lungs from chest X-ray images, breast cancer from ultrasound images, placental vessels from fetoscopic images, polyps from colonoscopy images, foot ulcers from standard camera images, intraretinal cystoid fluid from optical coherence tomography (OCT) images, and left ventricle and myocardial wall from echocardiography images, utilizing 16 datasets. Each dataset was randomly partitioned into training, validation, and test sets, with the corresponding statistics presented in Table 1.

For skin lesion segmentation from dermoscopy images, we utilized the ISIC2018 (38), PH2 (39), DermIS (40), and DermQuest (41) datasets. The ISIC2018 dataset, provided by the International Skin Imaging Collaboration (ISIC)

741 2018 Challenge, comprises 2,594 dermoscopy images,  
742 each meticulously annotated with pixel-level skin lesion  
743 labels. The PH2 dataset, acquired at the Dermatology  
744 Service of Hospital Pedro Hispano in Matosinhos, Por-  
745 tugal, contains 200 dermoscopic images of melanocytic  
746 lesions. These images are in 8-bit RGB color format with  
747 a resolution of 768x560 pixels. DermIS offers a compre-  
748 hensive collection of dermatological images covering a  
749 range of skin conditions, including dermatitis, psoriasis,  
750 eczema, and skin cancer. DermQuest includes 137 images  
751 representing two types of skin lesions: melanoma and nevus.

752  
753 For lung segmentation from chest X-rays, we utilized  
754 the JSRT (42), NLM-MC (43), NLM-SZ (43), and COVID-  
755 QU-Ex (44) datasets. The JSRT dataset consists of 247 chest  
756 X-ray images from Japanese patients, each accompanied by  
757 manually annotated ground truth masks that delineate the  
758 lung regions. The NLM-MC dataset was collected from the  
759 Department of Health and Human Services in Montgomery  
760 County, Maryland, USA. It includes 138 frontal chest  
761 X-rays, with manual lung segmentations provided. Of these,  
762 80 images represent normal cases, while 58 exhibit man-  
763 ifestations of tuberculosis (TB). The images are available  
764 in two resolutions: 4,020x4,892 pixels and 4,892x4,020  
765 pixels. The NLM-SZ dataset, sourced from Shenzhen No.3  
766 People's Hospital, Guangdong, China, contains 566 frontal  
767 chest X-rays in PNG format. Image sizes vary but are  
768 approximately 3,000x3,000 pixels. The COVID-QU-Ex  
769 dataset, compiled by researchers at Qatar University, com-  
770 prises a large collection of chest X-ray images, including  
771 11,956 COVID-19 cases, 11,263 non-COVID infections,  
772 and 10,701 normal instances. Ground-truth lung segmen-  
773 tation masks are provided for all images in this dataset.

774  
775 For placental vessel segmentation from fetoscopic images,  
776 we utilized the FPD (45) and FetReg (46) datasets. The FPD  
777 dataset comprises 482 frames extracted from six distinct  
778 in vivo fetoscopic procedure videos. To reduce redundancy and  
779 ensure a diverse set of annotated samples, the videos were  
780 down-sampled from 25 to 1 fps, and each frame was resized  
781 to a resolution of 448x448 pixels. Each frame is provided  
782 with a corresponding segmentation mask that precisely  
783 outlines the blood vessels. The FetReg dataset, developed  
784 for the FetReg2021 challenge, is the first large-scale, multi-  
785 center dataset focused on fetoscopy laser photocoagulation  
786 procedures. It contains 2,718 pixel-wise annotated images,  
787 categorizing background, vessel, fetus, and tool classes,  
788 sourced from 24 different in vivo TTTS fetoscopic surgeries.

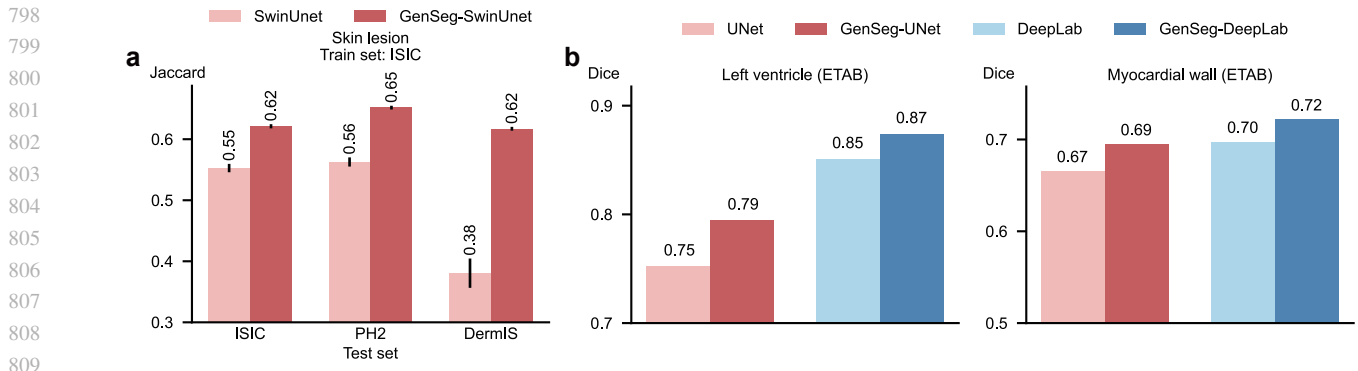
789  
790 For polyp segmentation from colonoscopic images, we  
791 utilized the KVASIR (47) and CVC-ClinicDB (48) datasets.  
792 Polyps are recognized as precursors to colorectal cancer  
793 and are detected in nearly half of individuals aged 50  
794 and older who undergo screening colonoscopy, with their  
795 prevalence increasing with age. Early detection of polyps  
796 significantly improves survival rates from colorectal cancer.

The KVASIR dataset was collected using endoscopic equip-  
ment at Vestre Viken Health Trust (VV) in Norway, which  
consists of four hospitals and provides healthcare services to  
a population of 470,000. The dataset includes images with  
varying resolutions, ranging from 720x576 to 1920x1072  
pixels. It contains 1,000 polyp images, each accompanied  
by a corresponding segmentation mask, with annotations  
verified by experienced endoscopists. CVC-ClinicDB  
comprises frames extracted from colonoscopy videos and  
consists of 612 images with a resolution of 384x288 pixels,  
derived from 31 colonoscopy sequences. videos.

For breast cancer segmentation, we utilized the BUID  
dataset (49), which consists of 630 breast ultrasound images  
collected from 600 female patients aged between 25 and 75  
years. The images have an average resolution of 500x500  
pixels. For foot ulcer segmentation, we utilized data from  
the FUSeg challenge (50), which includes over 1,000 images  
collected over a span of two years from hundreds of patients.  
The raw images were captured using Canon SX 620 HS  
digital cameras and iPad Pro under uncontrolled lighting  
conditions, with diverse backgrounds. For the segmentation  
of intraretinal cystoids from Optical Coherence Tomog-  
raphy (OCT) images, we utilized the Intraretinal Cystoid  
Fluid (ICFluid) dataset (51). This dataset comprises 1,460  
OCT images along with their corresponding masks for the  
Cystoid Macular Edema (CME) ocular condition. For the  
segmentation of left ventricles and myocardial wall, we  
employed data examples from the ETAB benchmark (52). It  
is constructed from five publicly available echocardiogram  
datasets, encompassing diverse cohorts and providing  
echocardiographies with a variety of views and annotations.

**Metrics.** For all segmentation tasks except skin lesion seg-  
mentation, we used the Dice score as the evaluation metric,  
adhering to established conventions in the field (53). The  
Dice score is calculated as  $\frac{2|A \cap B|}{|A| + |B|}$ , where  $A$  represents the  
algorithm's prediction and  $B$  denotes the ground truth. For  
skin lesion segmentation, we followed the guidelines of the  
ISIC challenge (54) and employed the Jaccard index, also  
known as intersection-over-union (IoU), as the performance  
metric. The Jaccard index is computed as  $\frac{|A \cap B|}{|A \cup B|}$  for each  
patient case. These metrics provide a robust assessment of  
the overlap between the predicted segmentation mask and  
the ground truth.

**Hyperparameters.** In our method, mask augmentation was  
performed using a series of operations, including rotation,  
flipping, and translation, applied in a random sequence. The  
mask-to-image generation model was based on the Pix2Pix  
framework (35), with an architecture that was made search-  
able, as depicted in Fig. 1b. The tradeoff parameter  $\gamma$  was set  
to 1. We configured the training process to perform 5,000  
iterations. The RMSprop optimizer (55) was utilized for  
training the segmentation model. It was set with an initial  
learning rate of  $1e-5$ , a momentum of 0.9, and a weight de-



**Extended Data Fig. 1** | **a**, Comparison between GenSeg-SwinUnet and SwinUnet models, both trained on 40 examples from the ISIC dataset and evaluated on the test sets of ISIC, PH2, and DermIS. **b**, The performance of GenSeg applied to UNet (GenSeg-UNet) and DeepLab (GenSeg-DeepLab) under in-domain settings (test and training data are from the same domain) in the tasks of segmenting left ventricles and myocardial wall using 8 training examples from the ETAB dataset, compared to vanilla UNet and DeepLab.

815 cay of  $1e-3$ . Additionally, the ReduceLRonPlateau scheduler was employed to dynamically adjust the learning rate according to the model's performance throughout the training period. Specifically, the scheduler was configured with a patience of 2 and set to 'max' mode, meaning it monitored the model's validation performance and adjusted the learning rate to maximize validation accuracy. For training the mask-to-image generation model, the Adam optimizer (56) was chosen, configured with an initial learning rate of  $1e-5$ , beta values of (0.5, 0.999), and a weight decay of  $1e-3$ . Adam was also applied for optimizing the architecture variables, with a learning rate of  $1e-4$ , beta values of (0.5, 0.999), and weight decay of  $1e-5$ . At the end of each epoch, we assessed the performance of the trained segmentation model on a validation set. The model checkpoint with the best validation performance was selected as the final model. The experiments were conducted on A100 GPUs, with each method being run three times using randomly initialized model weights. We report the average results along with the standard deviation across these three runs.

836 **The impact of the tradeoff parameter  $\lambda$  on segmentation performance.** We investigated the effect of the hyperparameter  $\lambda$  in Eq.(2) on the performance of our method. This parameter controls the balance between the contributions of real and generated data during the training of the segmentation model. Optimal performance was observed with a moderate  $\lambda$  value (e.g., 1), which effectively balanced the use of real and generated data (Extended Data Fig. 2a).

845 **The impact of mask augmentation operations on segmentation performance.** In GenSeg, the initial step involves applying augmentation operations to generate synthetic segmentation masks from real masks. We explored the impact of augmentation operations on segmentation performance. GenSeg, which utilizes all three operations - rotation, translation, and flipping - is compared against three specific ablation settings where only one operation (Rotate, Translate, or Flip) is used to augment the masks. GenSeg

demonstrated significantly superior performance compared to any of the individual ablation settings (Extended Data Fig. 2b). Notably, GenSeg exhibited superior generalization on out-of-domain data, highlighting the advantages of integrating multiple augmentation operations compared to using a single operation. By combining various augmentation operations, GenSeg can generate a broader diversity of augmented masks, which in turn produces a more diverse set of augmented images. Training segmentation models on this diverse dataset allows for learning more robust representations, thereby significantly enhancing generalization capabilities on out-of-domain test data.

**The impact of mask-to-image GANs on segmentation performance.** We investigated the impact of the mask-to-image conditional Generative Adversarial Network (GAN) in GegSeg on segmentation performance by comparing the default Pix2Pix model with two other conditional GAN models: SPADE (57) and ASAPNet (58). In this comparison, we made the architectures of these models' generators searchable. Pix2Pix and SPADE demonstrated comparable performance, both significantly outperforming ASAPNet (Extended Data Fig. 2c). This performance gap can be attributed to the superior image generation capabilities of Pix2Pix and SPADE.

**Computation costs.** Given that GenSeg is designed for scenarios with limited training data, the overall training time is minimal, often requiring less than 2 GPU hours (Extended Data Fig. 2d). To enhance the efficiency of GenSeg's training, we plan to incorporate strategies from (59, 60) for accelerated GAN training and implement the algorithm proposed in (61) to expedite the convergence of multi-level optimization. Importantly, our method does not increase the inference cost of the segmentation model. This is because our approach maintains the original architecture of the segmentation model, ensuring that the Multiply-Accumulate (MAC) operations remain unchanged.

## Data availability

Datasets used in this study are available at *ISIC*, *PH2*, *DermIS* and *DermQuest*, *JSRT*, *NLM-MC* and *NLM-SZ*, *COVID-QU-Ex Dataset*, *BUID*, *FPD*, *FetReg*, *KVASIR*, *CVC-Clinic*, *FUSed*, *ICFluid*, and *ETAB*.

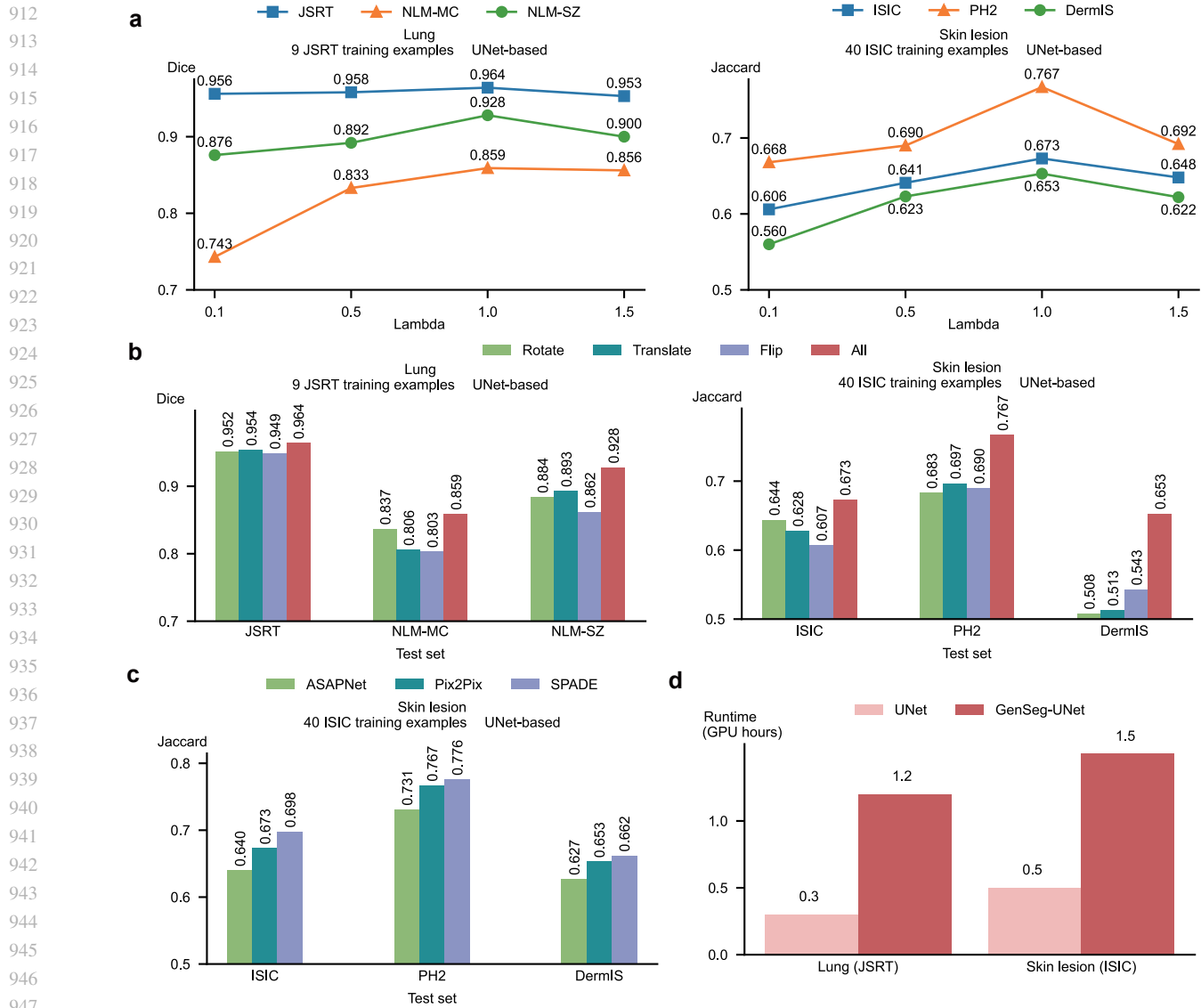
## Code availability

Our GenSeg code is available in the GitHub repository [https://github.com/importZL/semantic\\_segmentation](https://github.com/importZL/semantic_segmentation).

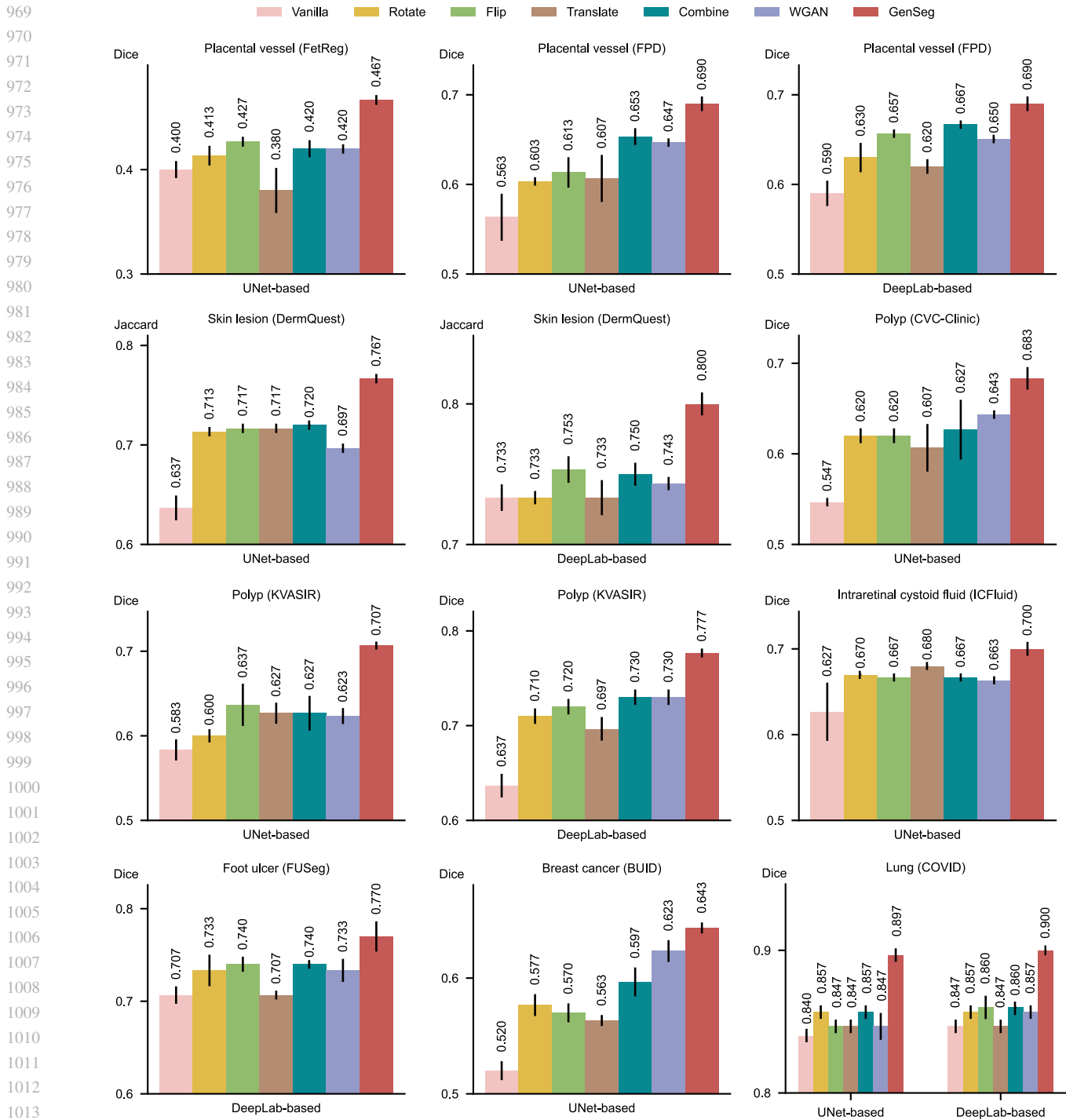
## References

- Mehdi Mirza and Simon Osindero. Conditional generative adversarial nets. *arXiv preprint arXiv:1411.1784*, 2014.
- Phillip Isola, Jun-Yan Zhu, Tinghui Zhou, and Alexei A Efros. Image-to-image translation with conditional adversarial networks. In *Proceedings of the IEEE conference on computer vision and pattern recognition*, pages 1125–1134, 2017.
- Hanxiao Liu, Karen Simonyan, and Yiming Yang. Darts: Differentiable architecture search. In *International Conference on Learning Representations*, 2019.
- Hanxiao Liu, Karen Simonyan, and Yiming Yang. Darts: Differentiable architecture search. In *International Conference on Learning Representations*, 2019.
- Noel Codella, Veronica Rotemberg, Philipp Tschandl, M Emre Celebi, Stephen Dusza, David Gutman, Brian Helba, Aadi Kaloo, Konstantinos Liopyris, Michael Marchetti, et al. Skin lesion analysis toward melanoma detection 2018: A challenge hosted by the international skin imaging collaboration (isic). *arXiv preprint arXiv:1902.03368*, 2019.
- Teresa Mendonca, Pedro M Ferreira, Jorge S Marques, Andre RS Marcal, and Jorge Rozeira. Ph<sup>2</sup>-a dermoscopic image database for research and benchmarking. In *Annual International Conference of the IEEE Engineering in Medicine and Biology Society*, volume 2013, pages 5437–5440, 2013.
- Jeffrey Luc Glaister. Automatic segmentation of skin lesions from dermatological photographs. Master's thesis, University of Waterloo, 2013.
- Audrey G Chung, Christian Scharfenberger, Farzad Khalvati, Alexander Wong, and Masoom A Haider. Statistical textural distinctiveness in multi-parametric prostate mri for suspicious region detection. In *International Conference Image Analysis and Recognition*, pages 368–376. Springer, 2015.
- Junji Shiraiishi, Shigehiko Katsuragawa, Junpei Ikezoe, Tsuneo Matsumoto, Takeshi Kobayashi, Ken-ichi Komatsu, Mitate Matsui, Hiroshi Fujita, Yoshie Koderu, and Kunio Doi. Development of a digital image database for chest radiographs with and without a lung nodule: receiver operating characteristic analysis of radiologists' detection of pulmonary nodules. *American Journal of Roentgenology*, 174(1):71–74, 2000.
- Stefan Jaeger, Sema Candemir, Sameer Antani, Yi-Xiang J Wang, Pu-Xuan Lu, and George Thoma. Two public chest x-ray datasets for computer-aided screening of pulmonary diseases. *Quantitative imaging in medicine and surgery*, 4(6):475, 2014.
- Anas M. Tahir, Muhammad E. H. Chowdhury, Yazan Qiblawey, Amith Khandakar, Tawsifur Rahman, Serkan Kiranyaz, Uzair Khurshid, Nabil Ibtehad, Sakib Mahmud, and Maymouna Ezeddin. Covid-qu-ex dataset, 2022.
- Sophia Bano, Francisco Vasconcelos, Luke M Shepherd, Emmanuel Vander Poorten, Tom Vercauteren, Sebastien Ourselin, Anna L David, Jan Deprest, and Danail Stoyanov. Deep placental vessel segmentation for fetoscopic mosaicking. In *Medical Image Computing and Computer Assisted Intervention—MICCAI: 23rd International Conference*, pages 763–773. Springer, 2020.
- Sophia Bano, Alessandro Casella, Francisco Vasconcelos, Sara Moccia, George Attilakos, Ruwan Wimalasundera, Anna L David, Dario Paladini, Jan Deprest, Elena De Momi, et al. Fetreg: placental vessel segmentation and registration in fetoscopy challenge dataset. *arXiv preprint arXiv:2106.05923*, 2021.
- Debesh Jha, Pia H Smedsrud, Michael A Riegler, Pål Halvorsen, Thomas de Lange, Dag Johansen, and Håvard D Johansen. Kvasir-seg: A segmented polyp dataset. In *International Conference on Multimedia Modeling*, pages 451–462. Springer, 2020.
- Jorge Bernal, F Javier Sánchez, Gloria Fernández-Esparrach, Debora Gil, Cristina Rodríguez, and Fernando Vilarinho. Wm-dova maps for accurate polyp highlighting in colonoscopy: Validation vs. saliency maps from physicians. *Computerized medical imaging and graphics*, 43:99–111, 2015.
- Walid Al-Dhabyani, Mohammed Gomaa, Hussien Khaled, and Aly Fahmy. Dataset of breast ultrasound images. *Data in brief*, 28:104863, 2020.
- Chuanbo Wang, DM Anisuzzaman, Victor Williamson, Mrinal Kanti Dhar, Behrouz Rostami, Jeffrey Niezgoda, Sandeep Gopalakrishnan, and Zeyun Yu. Fully automatic wound segmentation with deep convolutional neural networks. *Scientific reports*, 10(1):21897, 2020.
- Zeeshan Ahmed, Munawar Ahmed, Attiya Baqai, and Fahim Aziz Umrani. Intraretinal cystoid fluid, 2022.
- Ahmed M Alaa, Anthony Philippakis, and David Sontag. Etab: A benchmark suite for visual representation learning in echocardiography. *Advances in Neural Information Processing Systems*, 35:19075–19086, 2022.
- Jeroen Bertels, Tom Eelbode, Maxim Berman, Dirk Vandermeulen, Frederik Maes, Raf Bisschops, and Matthew B Blaschko. Optimizing the dice score and jaccard index for medical image segmentation: Theory and practice. In *Medical Image Computing and Computer Assisted Intervention—MICCAI: 22nd International Conference*, pages 92–100. Springer, 2019.
- Veronica Rotemberg, Nicholas Kurtansky, Brigid Betz-Stablein, Liam Caffery, Emmanouil Chousakos, Noel Codella, Marc Combalia, Stephen Dusza, Pascale Guitera, David Gutman, et al. A patient-centric dataset of images and metadata for identifying melanomas using clinical context. *Scientific data*, 8(1):34, 2021.
- Naichen Shi and Dawei Li. Rmsprop converges with proper hyperparameter. In *International conference on learning representation*, 2021.
- Diederik Kingma and Jimmy Ba. Adam: A method for stochastic optimization. In *International Conference on Learning Representations*, 2015.
- Taesung Park, Ming-Yu Liu, Ting-Chun Wang, and Jun-Yan Zhu. Semantic image synthesis with spatially-adaptive normalization. In *Proceedings of the IEEE/CVF conference on computer vision and pattern recognition*, pages 2337–2346, 2019.
- Tamar Rott Shaham, Michaël Gharbi, Richard Zhang, Eli Shechtman, and Tomer Michaeli. Spatially-adaptive pixelwise networks for fast image translation. In *Proceedings of the IEEE/CVF conference on computer vision and pattern recognition*, pages 14882–14891, 2021.
- Samarth Sinha, Han Zhang, Anirudh Goyal, Yoshua Bengio, Hugo Larochelle, and Augustus Odena. Small-gan: Speeding up gan training using core-sets. In *International Conference on Machine Learning*, pages 9005–9015. PMLR, 2020.
- Samarth Sinha, Zhengli Zhao, Anirudh Goyal ALIAS PARTH GOYAL, Colin A Raffel, and Augustus Odena. Top-k training of gans: Improving gan performance by throwing away bad samples. *Advances in Neural Information Processing Systems*, 33:14638–14649, 2020.
- Ryo Sato, Mirai Tanaka, and Akiko Takeda. A gradient method for multilevel optimization. *Advances in Neural Information Processing Systems*, 34:7522–7533, 2021.

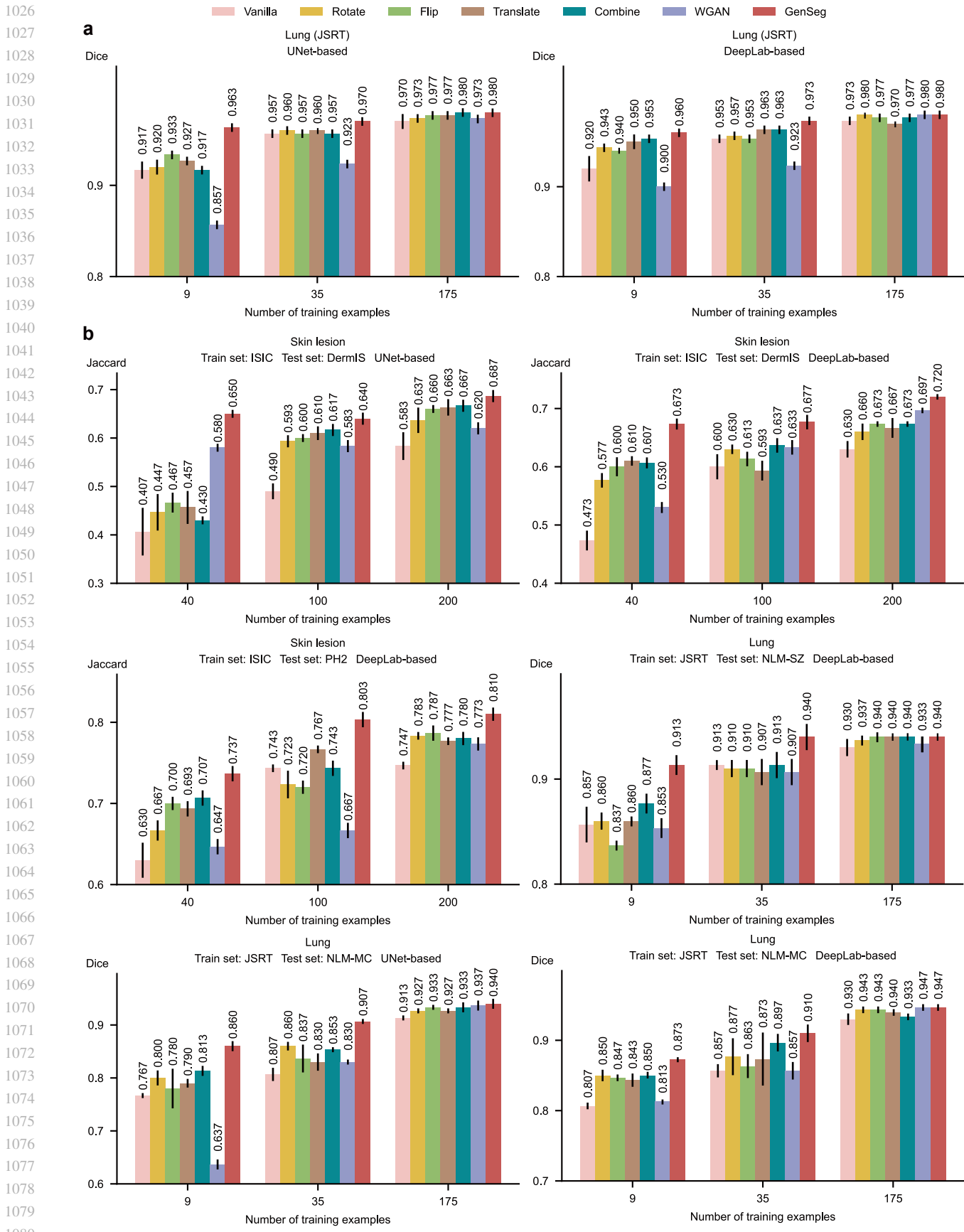




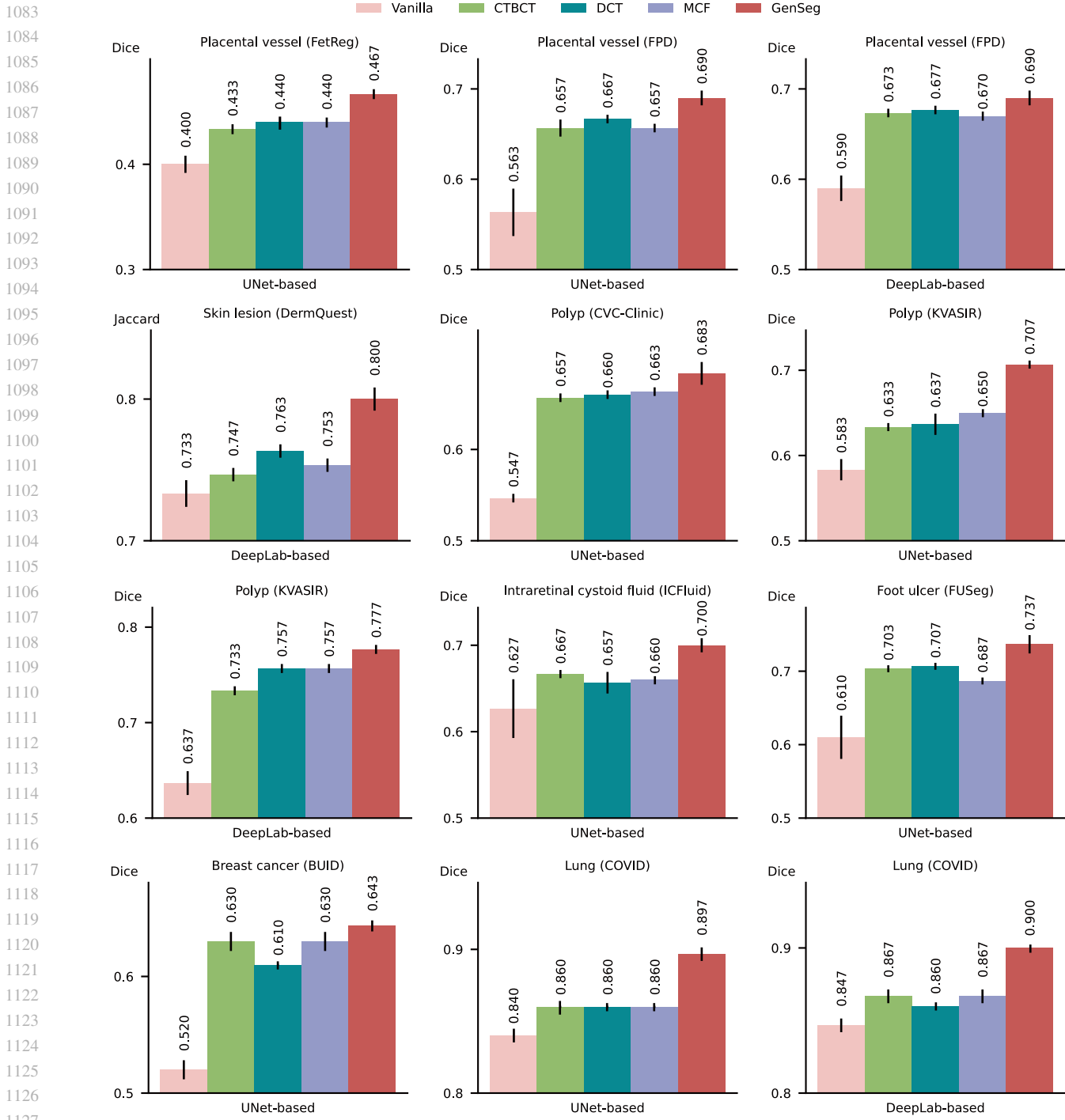
**Extended Data Fig. 2** | **a**, (Left) Impact of the tradeoff parameter  $\lambda$  on the performance of GenSeg-UNet was evaluated on the test datasets of JSRT, NLM-MC, and NLM-SZ, in lung segmentation. GenSeg-UNet was trained using 9 examples from the JSRT training dataset. (Right) Impact of the tradeoff parameter  $\lambda$  on the performance of GenSeg-UNet was evaluated on the test datasets of ISIC, PH2, and DermIS, in skin lesion segmentation. GenSeg-UNet was trained using 40 examples from the ISIC training dataset. **b**, (Left) Impact of augmentation operations on the performance of GenSeg-UNet was evaluated on the test datasets of JSRT, NLM-MC, and NLM-SZ, in lung segmentation. GenSeg-UNet was trained using 9 examples from the JSRT training dataset. *All* refers to the full GenSeg method that incorporates all three operations. (Right) Impact of augmentation operations on the performance of GenSeg-UNet was evaluated on the test datasets of ISIC, PH2, and DermIS, in skin lesion segmentation. GenSeg-UNet was trained using 40 examples from the ISIC training dataset. **c**, Impact of mask-to-image GAN models on the performance of GenSeg-UNet was evaluated on the test datasets of ISIC, PH2, and DermIS, in skin lesion segmentation. GenSeg-UNet was trained using 40 examples from the ISIC training dataset. **d**, The runtime (in hours on an A100 GPU) of GenSeg-UNet was measured for lung segmentation using JSRT as the training data and for skin lesion segmentation using ISIC as the training data.



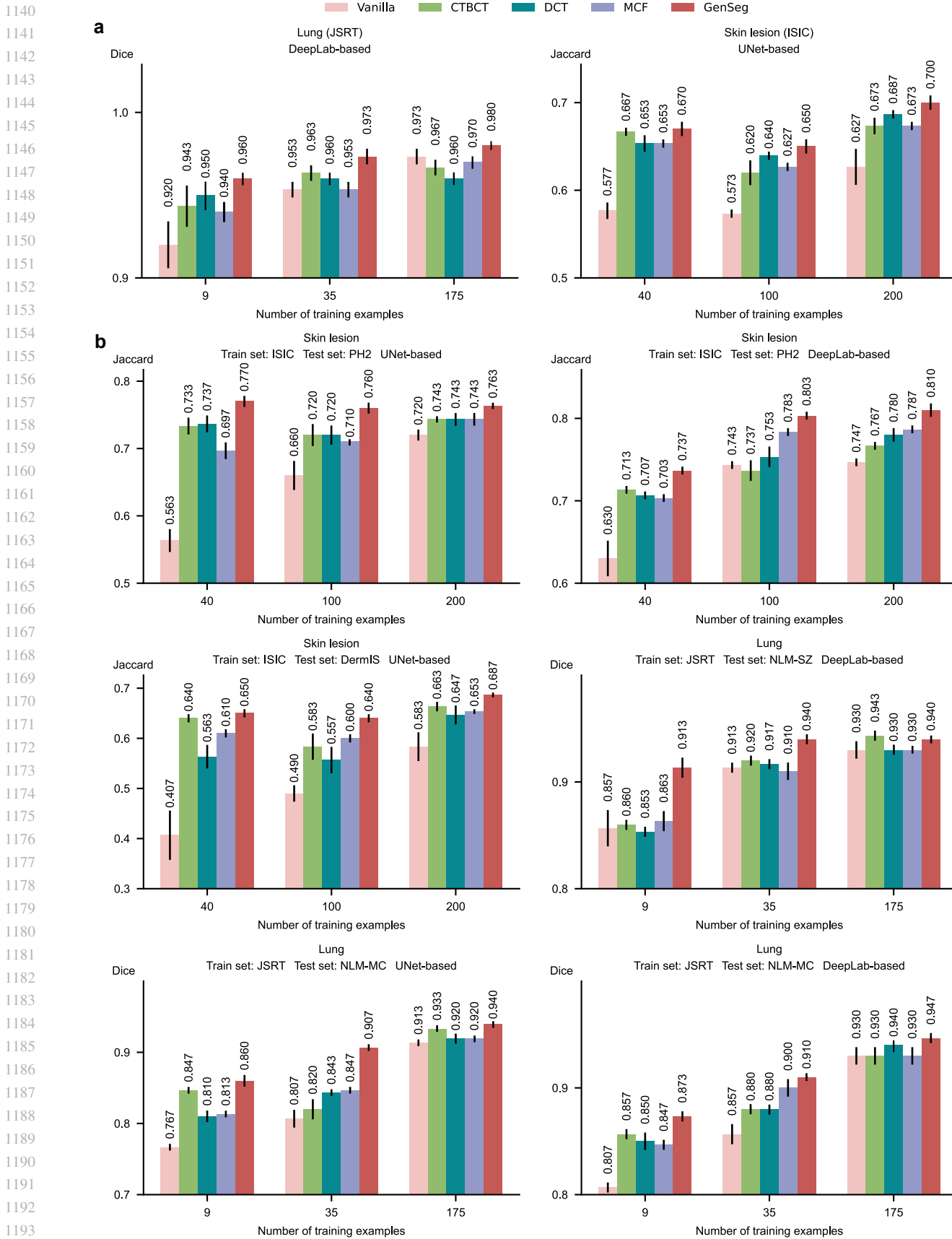
**Extended Data Fig. 3 | Further comparison of GegSeg with data augmentation and generation methods.** GenSeg's in-domain generalization performance compared to baseline methods including Rotate, Flip, Translate, Combine, and WGAN, when used with UNet or DeepLab in segmenting placental vessels, skin lesions, polyps, intraretinal cystoid fluids, foot ulcers, breast cancer, and lungs, using the FetReg, FPD, DermQuest, CVC-Clinic, KVASIR, ICFluid, FUSeg, BUID, and COVID datasets.



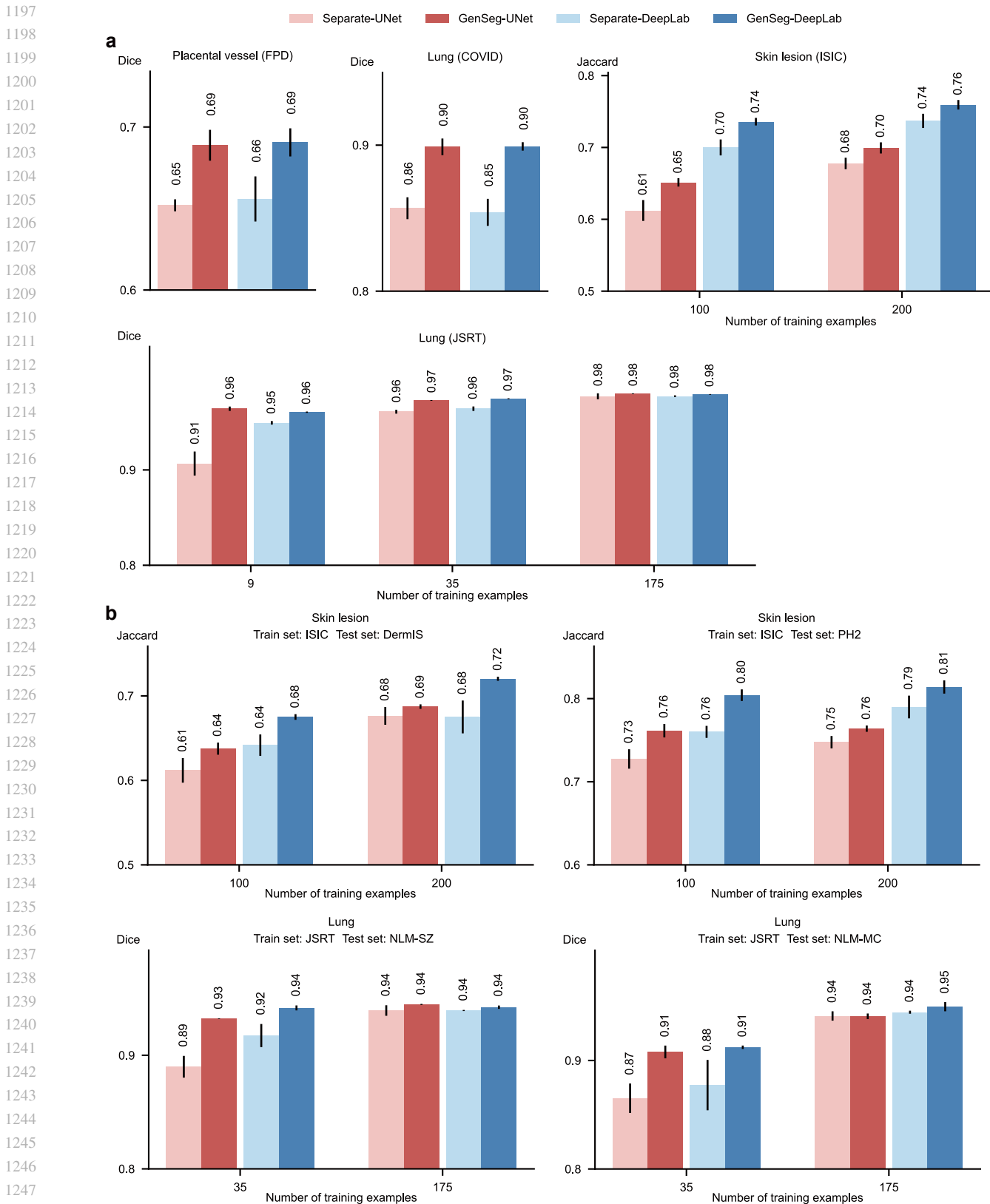
**Extended Data Fig. 4 | Further comparison of GegSeg with data augmentation and generation methods across varying numbers of training examples. a**, Comparison of in-domain generalization performance for lung segmentation using the JSRT dataset. **b**, Comparison of out-of-domain generalization performance in segmenting skin lesions (using the ISIC dataset for training, DermIS and PH2 for testing) and lungs (using JSRT for training, NLM-SZ and NLM-MC for testing).



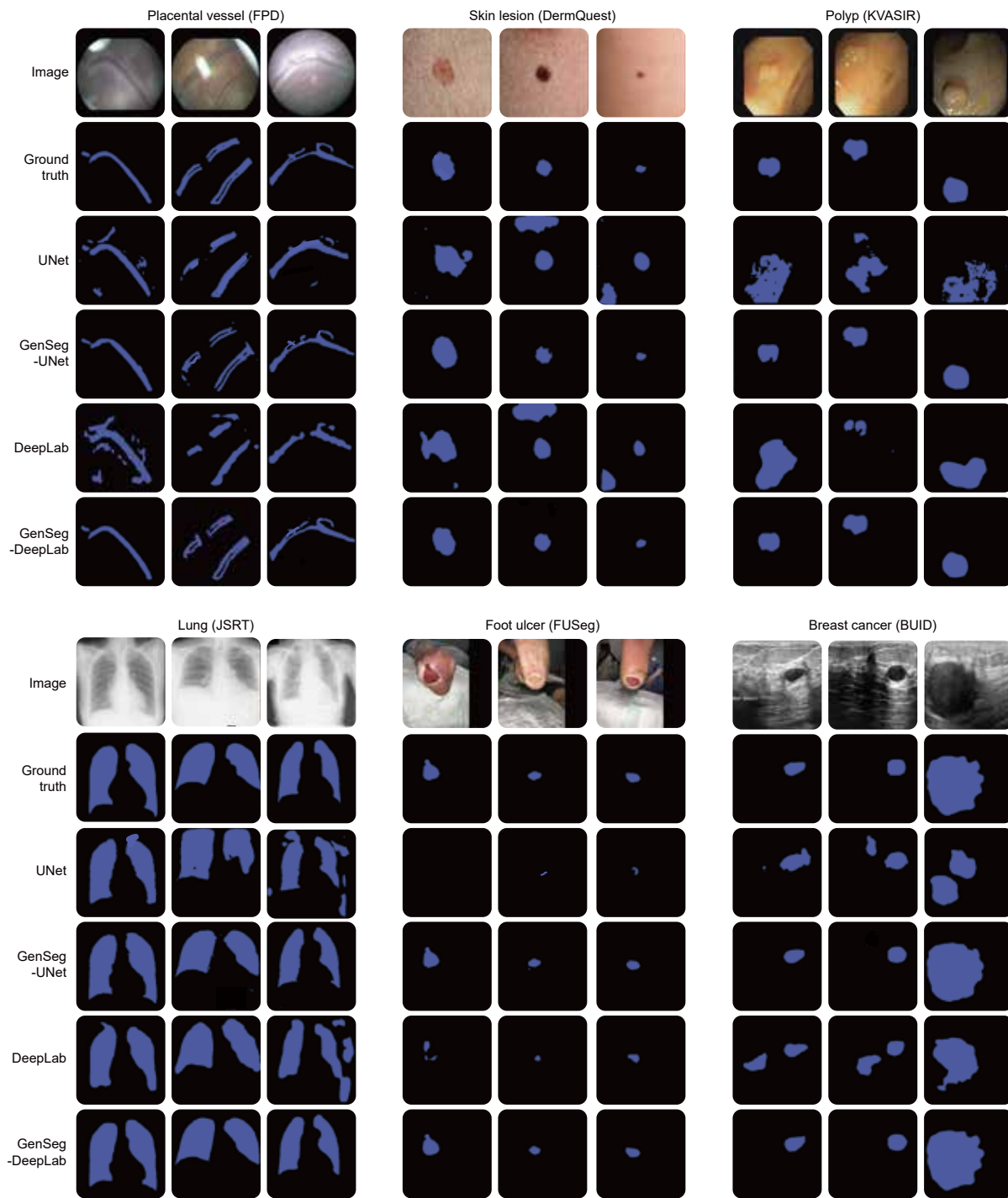
**Extended Data Fig. 5 | Further comparison of GegSeg with semi-supervised segmentation methods.** GenSeg's in-domain generalization performance compared to baseline methods including CTBCT, DCT, and MCF, when used with UNet or DeepLab in segmenting placental vessels, skin lesions, polyps, intraretinal cystoid fluids, foot ulcers, breast cancer, and lungs utilizing the FetReg, FPD, DermQuest, CVC-Clinic, KVASIR, ICFluid, FUSeg, BUID, and COVID datasets.



**Extended Data Fig. 6 | Further comparison of GegSeg with semi-supervised segmentation methods across varying numbers of training examples. a**, Comparison of in-domain generalization performance for segmenting lungs (using the JSRT dataset) and skin lesions (using ISIC). **b**, Comparison of out-of-domain generalization performance for segmenting skin lesions (using ISIC for training, and PH2 and DermIS for testing) and lungs (using JSRT for training, and NLM-SZ and NLM-MC for testing).

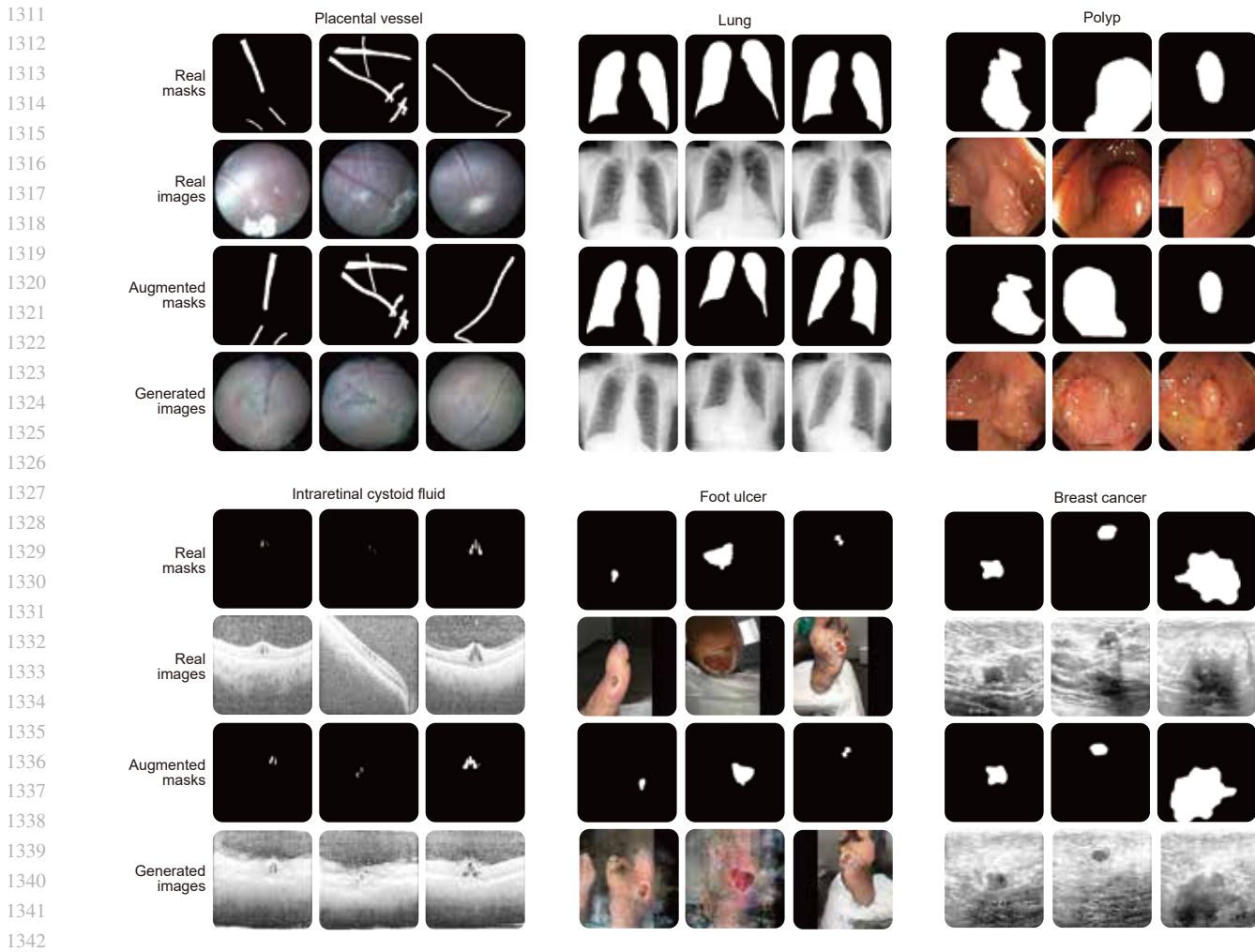


**Extended Data Fig. 7 | Further comparison of GenSeg's end-to-end data generation mechanism with baselines' separate generation mechanism. a**, GenSeg's end-to-end generation mechanism greatly improves models' in-domain generalization performance, when used UNet and DeepLab in segmenting placental vessels, lung regions, and skin lesions using FPD, COVID, ISIC, and JSRT datasets. **b**, GenSeg's end-to-end generation mechanism greatly improves models' out-of-domain generalization performance, when used UNet and DeepLab in segmenting skin lesions (using ISIC for training, and DermIS and PH2 for testing), and lung regions (using JSRT for training, and NLM-SZ and NLM-MC for testing).



Extended Data Fig. 8 | Additional visualizations of predicted segmentation masks.

1254  
1255  
1256  
1257  
1258  
1259  
1260  
1261  
1262  
1263  
1264  
1265  
1266  
1267  
1268  
1269  
1270  
1271  
1272  
1273  
1274  
1275  
1276  
1277  
1278  
1279  
1280  
1281  
1282  
1283  
1284  
1285  
1286  
1287  
1288  
1289  
1290  
1291  
1292  
1293  
1294  
1295  
1296  
1297  
1298  
1299  
1300  
1301  
1302  
1303  
1304  
1305  
1306  
1307  
1308  
1309  
1310



1343 **Extended Data Fig. 9 | Visualizations of image-mask pairs generated by GenSeg.** Synthetic segmentation masks and medical images generated by GenSeg in tasks  
1344 of segmenting placental vessels, lungs, polyps, intraretinal cystoid fluid, foot ulcers, and breast cancer.

1345  
1346  
1347  
1348  
1349  
1350  
1351  
1352  
1353  
1354  
1355  
1356  
1357  
1358  
1359  
1360  
1361  
1362  
1363  
1364  
1365  
1366  
1367